JℲM PAPERS

Bubble–particle collisions in turbulence: insights from point-particle simulations

Timothy T.K. Chan[1],†, **Chong Shen Ng**[1] **and Dominik Krug**[1],†

[1]Physics of Fluids Group, Max Planck Center Twente for Complex Fluid Dynamics, Faculty of Science and Technology, MESA+ Research Institute, and J. M. Burgers Centre for Fluids Dynamics, University of Twente, P.O. Box 217, 7500 AE Enschede, The Netherlands

Bubble–particle collisions in turbulence are central to a variety of processes such as froth flotation. Despite their importance, details of the collision process have not received much attention yet. This is compounded by the sometimes counter-intuitive behaviour of bubbles and particles in turbulence, as exemplified by the fact that they segregate in space. Although bubble–particle relative behaviour is fundamentally different from that of identical particles, the existing theoretical models are nearly all extensions of theories for particle–particle collisions in turbulence. The adequacy of these theories has yet to be assessed as appropriate data remain scarce to date. In this investigation, we study the geometric collision rate by means of direct numerical simulations of bubble–particle collisions in homogeneous isotropic turbulence using the point-particle approach over a range of the relevant parameters, including the Stokes and Reynolds numbers. We analyse the spatial distribution of bubble and particles, and quantify to what extent their segregation reduces the collision rate. This effect is countered by increased approach velocities for bubble–particle compared to monodisperse pairs, which we relate to the difference in how bubbles and particles respond to fluid accelerations. We found that in the investigated parameter range, these collision statistics are not altered significantly by the inclusion of a lift force or different drag parametrisations, or when assuming infinite particle density. Furthermore, we critically examine existing models and discuss inconsistencies therein that contribute to the discrepancy.

Key words: bubble dynamics, particle/fluid flow

† Email addresses for correspondence: t.k.t.chan@utwente.nl, d.j.krug@utwente.nl

1. Introduction

Collisions between bubbles and particles in a turbulent flow are of significant technological relevance. In particular, such collisions are essential to the flotation process, which is a widely used separation technique especially in the mining industry (Nguyen & Schulze 2004). In this process, after grinding, small ore fragments are fed into a big water-filled cell that is agitated via a rotor and into which air bubbles are injected. Collisions between the ore particles and the bubbles then form the base for the decisive test: valuable mineral particles attach to the bubbles due to their hydrophobic surface and consequently rise to the top where they can be skimmed off as a froth, whereas the hydrophilic waste rock particles remain in suspension and are eventually discharged as tailings. This technology is already applied at staggering scales (Nguyen & Schulze (2004) estimated that a total of 2 billion tons of ore are treated annually). Given especially the relevance in the mining of copper, and in view of the strong push for electrification in response the the climate crisis, these numbers are likely to continue to rise in the future (Rogich & Matos 2008; World Bank Group 2017). The interest to understand the collision process better is driven by the demand for more reliable process modelling (Kostoglou, Karapantsios & Evgenidis 2020a) but also by the need for performance improvement. The latter is especially a concern for small particles with diameters smaller than 20 μm, where recovery is poor owing to their low collision rates (Nguyen, George & Jameson 2006; Miettinen, Ralston & Fornasiero 2010).

For modelling purposes, the collision process is generally separated into two components (Pumir & Wilkinson 2016): the 'geometric collision rate', which considers the collisions neglecting any interaction between the collision partners, and the 'collision efficiency', which quantifies how many of these collisions actually happen when taking the local modification of the flow field into account. The focus here is on the (ensemble-averaged) geometric collision rate between two species, '1' and '2', which when expressed per unit volume can be written as

$$Z_{12} = \Gamma_{12} n_1 n_2, \tag{1.1}$$

where Γ_{12} is the collision kernel, and n_1 and n_2 denote the respective number densities of the two species. The collision kernel measures the rate at which the separation vector between particle centres crosses the collision distance. For spherical particles with a collision distance $r_c = r_1 + r_2$ (where r_1, r_2 denote the particle radii), Γ_{12} can be expressed as (Sundaram & Collins 1997)

$$\Gamma_{12} = 4\pi r_c^2 \, g(r_c) \, S_-(r_c), \tag{1.2}$$

where besides the surface area $4\pi r_c^2$ of the collision sphere, the other factors are the radial distribution function (RDF) at collision distance $g(r_c)$, which describes variations in the local particle concentration, and the effective radial approach velocity at contact,

$$S_-(r_c) = - \int_{-\infty}^{0} \Delta v_r \text{p.d.f.}(\Delta v_r | r_c) \, \mathrm{d}(\Delta v_r). \tag{1.3}$$

Here, Δv_r is the radial component of the relative velocity, which is positive when the pair separates, and p.d.f.$(\Delta v_r | r_c)$ is the probability density function of Δv_r conditioned on a pair with separation r_c.

The bidisperse collision kernel Γ_{12} depends on a multitude of parameters characterising properties of the suspended particles and of the carrier flow. The discussion here is

restricted to homogeneous isotropic turbulence for which the most relevant dependencies may be summarised in non-dimensional form as

$$\frac{\Gamma_{12}}{r_c^3/\tau_\eta} = f\left(St_1, St_2, \frac{\rho_1}{\rho_f}, \frac{\rho_2}{\rho_f}, Re_\lambda, \frac{r_1}{\eta}, \frac{r_2}{\eta}, Fr, \dots\right). \tag{1.4}$$

Here, the Stokes number

$$St_i = \frac{\tau_i}{\tau_\eta} = \frac{r_i^2(2\rho_i/\rho_f + 1)}{9\nu\tau_\eta}, \tag{1.5}$$

($i = 1, 2$) characterises how well particles follow the flow by relating the particle response time $\tau_i = r_i^2(2\rho_i/\rho_f + 1)/(9\nu)$ to the Kolmogorov time scale of the turbulence $\tau_\eta = (\nu/\varepsilon)^{1/2}$, with ν and ε denoting the kinematic viscosity and the average rate of turbulent dissipation, respectively. Further, the ratios of particle (ρ_i) and fluid (ρ_f) densities are relevant as they characterise to what extent the particle motion is influenced by fluid ('added mass') inertia and buoyancy. The particle radii r_i determine the collision radius r_c, and their size relative to the Kolmogorov length scale $\eta = (\nu^3/\varepsilon)^{1/4}$ determines the range of turbulent scales relevant for their motion. In addition to turbulent driving, particle motion may also be affected by gravitational effects, and the relative importance of these two factors is captured by the Froude number $Fr = a_\eta/g$, where $a_\eta = \eta/\tau_\eta^2$ and g are the turbulence and gravitational accelerations, respectively. Finally, the intensity of the turbulence is measured by the Taylor Reynolds number $Re_\lambda = \sqrt{15/(\nu\varepsilon)}\, u'^2$, where u' is the single-component root-mean-square (r.m.s.) fluid velocity. Obviously, the entire parameter space spanned by (1.4) is vast and cannot be studied comprehensively here. We therefore limit the present investigation to cases with $St_1 = St_2 = St$, and to the zero-gravity regime, i.e. $Fr \to \infty$. The benefit of these choices lies in the fact that they keep the problem simple enough to disentangle the relevant mechanisms. Similarly, these configurations are the most amenable to modelling approaches and therefore allow for their evaluation at the most basic level.

Our investigation is based on direct numerical simulations of bubbles and particles in statistically stationary homogeneous isotropic turbulence using the point-particle approach. Details of this approach will be described in § 3 after first reviewing relevant modelling approaches for the collision kernel in § 2. The results are shown in § 4, followed in § 5 by practical considerations in light of our results, and conclusions.

2. Theoretical background and existing models

2.1. *The tracer limit $St \to 0$: shear mechanism*

In the tracer limit of $St \to 0$, the suspended species follow the flow faithfully and distribute uniformly. This means that collisions occur only if particles of finite size are moved relative to each other due to shearing motions in the flow. Considering the dominant shear contribution of the smallest (Kolmogorov) scales of turbulence, and assuming local isotropy as well as Gaussian distribution of the flow velocity gradient, Saffman & Turner (1956) derived the classical result

$$\Gamma_{12}^{(ST)} = \sqrt{\frac{8\pi}{15}} \frac{r_c^3}{\tau_\eta}, \tag{2.1}$$

predicting the rate of shear-driven collisions in a turbulent flow. Note that here we use the spherical formulation for the collision kernel, which was shown to be the appropriate form

by Wang, Ayala & Xue (2005). Employing the concept of a collision cylinder, instead, results in a slightly different value of the prefactor ($\sqrt{8\pi}/3 \approx 1.67$ instead of $\sqrt{8\pi/15} \approx 1.29$).

2.2. *Intermediate St: preferential sampling and velocity decorrelation*

For non-zero *St*, the suspended species no longer completely follow the flow. Such inertial effects influence the collision rate via two different pathways. First, even if the drift is small, its accumulated effect leads to preferential concentration, inducing clustering in the particle field. Additionally, the increasing decorrelation between the local particle and fluid velocities affects the collision velocities.

Preferential concentration of inertial particles is widely observed experimentally (Aliseda *et al.* 2002; Monchaux, Bourgoin & Cartellier 2010; Obligado *et al.* 2014; Petersen, Baker & Coletti 2019; Li *et al.* 2021) and numerically (Bec *et al.* 2007; Goto & Vassilicos 2006; Calzavarini *et al.* 2008*b*; Voßkuhle *et al.* 2014; Ireland, Bragg & Collins 2016). It is rather straightforward to extend (2.1) to account for this effect by simply multiplying it with the RDF $g_{12}(r_c)$ (Voßkuhle *et al.* 2014), yielding

$$\Gamma_{12}^{(STc)} = \sqrt{\frac{8\pi}{15}} \frac{r_c^3}{\tau_\eta} g_{12}(r_c). \tag{2.2}$$

Various approaches have been proposed to explain the phenomenon of preferential concentration (Maxey 1987; Bec *et al.* 2005, 2007; Chen, Goto & Vassilicos 2006; Goto & Vassilicos 2006; Coleman & Vassilicos 2009; Zaichik & Alipchenkov 2009; Fouxon 2012). Among these, the most intuitive one is the 'centrifuge picture' (Maxey 1987), according to which heavy particles are ejected out of eddies due to their inertia and hence accumulate in regions of low vorticity and high strain. For collisions between heavy particles (e.g. cloud droplets), it is therefore found that $g_{12}(r_c) \geq 1$ generally (Zhou, Wexler & Wang 2001), i.e. clustering enhances the collision rate in some cases even by multiple orders of magnitude (Voßkuhle *et al.* 2014; Ireland *et al.* 2016; Pumir & Wilkinson 2016).

For the collision velocity, inertial effects can be split into a local mechanism and a non-local mechanism. The local mechanism results from the fact that particles react differently to the same fluid forcing provided that they have different properties. Hence this effect contributes an additional relative velocity for bidispersed collisions only, and plays no role in monodispersed cases. For this to occur, the particle trajectories should not deviate significantly from the pathlines (i.e. *St* not too large). An extension of the Saffman–Turner approach accounting for this effect has been reported by Yuu (1984).

In contrast, the non-local mechanism refers to the situation in which particles arrive at the same location with different particle velocities. Illustratively, one can think of these particles as being 'slung out' of neighbouring eddies, and the effect is therefore also known as the 'sling effect' (Falkovich, Fouxon & Stepanov 2002). Unlike the local mechanism, the sling effect is also active for monodisperse suspensions, and so far has been studied almost exclusively in this context (e.g. Falkovich *et al.* 2002; Wilkinson, Mehlig & Bezuglyy 2006; Falkovich & Pumir 2007; Ijzermans, Meneguz & Reeks 2010; Bewley, Saw & Bodenschatz 2013; Voßkuhle *et al.* 2014). From these studies, it has become clear (see e.g. Pumir & Wilkinson 2016, for an overview) that the sling effect can significantly enhance monodisperse collision rates by increasing S_-. A widely used parametrisation is $S_- \sim u_\eta F(St, Re_\lambda)$, where $u_\eta = \eta/\tau_\eta$ is the Kolmogorov velocity, such

that the sling-induced collision rate is given by

$$\Gamma_{11}^{(slg)} = 4\pi r_c^2 u_\eta \, F(St, Re_\lambda). \tag{2.3}$$

It has then been proposed (Wilkinson *et al.* 2006; Voßkuhle *et al.* 2014) to obtain the overall collision rate from the sum

$$\Gamma_{11}^{(tot)} = \Gamma_{11}^{(STc)} + \Gamma_{11}^{(slg)}. \tag{2.4}$$

The underlying idea for this decomposition is that particles that are clustered close to each other collide with low velocities, whereas those with high relative velocities can be assumed to be uniformly distributed. Note that both (2.3) and (2.4) are given for the monodisperse case only, since related results for the bidisperse case have not been reported yet.

2.3. *Large St limit: kinetic gas behaviour*

At very large (but finite) *St*, the velocities of the suspended particles arriving at the same point are increasingly uncorrelated. Assuming entirely random and isotropic particle velocities in the spirit of the kinetic gas theory, Abrahamson (1975) derived the collision kernel

$$\Gamma_{12}^{(A)} = \sqrt{8\pi} \, r_c^2 \sqrt{v_1'^2 + v_2'^2}, \tag{2.5}$$

where the mean-square single-component particle velocity $v_i'^2$ is related to flow properties via

$$v_i'^2 = A_i u'^2 = \frac{\dfrac{T_{fL}}{\tau_i} + \gamma_i^2}{\dfrac{T_{fL}}{\tau_i} + 1} \, u'^2, \tag{2.6}$$

with T_{fL} denoting the fluid Lagrangian integral time scale, and $\gamma_i = 3\rho_f/(2\rho_i + \rho_f)$. It has been pointed out (Voßkuhle *et al.* 2014) that (2.5) is not strictly valid for turbulence as it fails to account for the multiscale structure of the flow. Alternative derivations (Völk *et al.* 1980; Mehlig, Uski & Wilkinson 2007) based on the Kolmogorov (1941) phenomenology arrived at $F(St, \infty) \sim K\sqrt{St}$, with K being a universal dimensionless constant, at the limit of intense turbulence in the context of (2.3).

2.4. *Modelling approaches for bubble–particle collisions in turbulence*

Next, we outline briefly the different approaches to modelling bubble–particle collisions reported in particular in the mining literature so far. For additional details, we refer the reader to the reviews on the topic (e.g. Nguyen *et al.* 2016; Hassanzadeh *et al.* 2018; Kostoglou, Karapantsios & Oikonomidou 2020*b*). Note that here and in the following we use subscripts $i = b, p$ to denote bubbles and heavy particles, respectively.

The most commonly adopted approach is to assume the high-*St* limit and to base the collision models on (2.5). The differences from the theory of Abrahamson (1975) are related to the expressions used to model the r.m.s. velocities. Instead of (2.6), Schubert (1999) and later Bloom & Heindel (2002) used the relation given by Liepe & Möckel

(1976), which reads

$$w_i'^{(LM)} = 0.57 \, \frac{\varepsilon^{4/9} r_i^{7/9}}{\nu^{1/3}} \left(\frac{\rho_f - \rho_i}{\rho_f} \right)^{2/3}. \tag{2.7}$$

This result is based on an analogy to gravitational settling with the fluid acceleration in the inertial range replacing gravity. The resulting apparent weight is balanced by Allen's drag, which scales with the particle slip velocity $w_i = v_i - u$ as $|w_i|^{3/2}$ (with boldface denoting vectors). Here, v_i is the bubble/particle velocity, and u is the flow velocity. Later work by Nguyen & Schulze (2004) used (2.7) with a different constant, 0.83, for bubbles. For particles, they replaced the inertial subrange acceleration with that in the dissipation range, and Allen's drag with Stokes drag, in order to account for the small size of typical particles. This resulted in

$$w_p'^{(NS)} = \frac{2 r_p^3 \varepsilon}{135 \nu^2} \left(\frac{\rho_p - \rho_f}{\rho_f} \right). \tag{2.8}$$

Importantly, both (2.7) and (2.8) are expressions for the relative velocity between bubbles/particles and the surrounding fluid. Their use with Abrahamson's theory is therefore inconsistent since (2.5) contains velocities in a fixed frame of reference. This was already pointed out in Kostoglou *et al.* (2020*a*). We further note that the quasi-static assumption underlying (2.7) and (2.8) is equivalent to a low-*St* approximation and therefore not valid for the high-*St* limit in which (2.5) applies. In fact, (2.8) is consistent with the rigorously derived small-*St* limit (Fouxon 2012)

$$w_i = \beta_i \tau_i a_f, \tag{2.9}$$

with

$$\beta_i = \frac{2(\rho_f - \rho_i)}{\rho_f + 2\rho_i}, \tag{2.10}$$

if the fluid acceleration is approximated by the dissipative scaling $|a_f| \approx \varepsilon r_i / (15\nu)$. Note, however, that it appears more appropriate to use $|a_f| \approx a_\eta$ for small particles ($r_i/\eta \lesssim 1$) because $|a_f| \to 0$ otherwise. In the general case, the fact that the fluid acceleration experienced by the particle may vary considerably over the particle response time precludes a simple relation between w_i and a_f.

In a different approach, Ngo-Cong, Nguyen & Tran-Cong (2018) extended the model by Yuu (1984) to the bubble–particle case. The resulting expression takes the form

$$\Gamma_{bp}^{(NC)} = (r_b + r_p)^2 \sqrt{\frac{8\pi}{3} \left\{ 3(A_b + A_p - 2B) u'^2 + (A_b r_b^2 + A_p r_p^2 + 2B r_p r_b) \frac{\varepsilon}{3\nu} \right\}}, \tag{2.11}$$

where the term proportional to u'^2 represents the 'local' inertial effect on the relative velocity that adds to the shear-driven collisions that are accounted for by the ε term. Aside from bubble/particle properties, the coefficients A_i and B depend also on T_{fL}, similar to (2.6). The bubble–particle velocity correlation is determined by B. Ngo-Cong *et al.* (2018) additionally incorporated (2.7) and (2.8) into this model. However, doing so suffers from the same inconsistencies outlined above. As a consequence, this expression featured a negative radicand when evaluated for the parameters in this study, and is therefore not included further. It is worth mentioning that the term proportional to u'^2 in (2.11) does not approach (2.5) even at large *St*, since $A_i = B$ for identical particles. We have therefore extended the model along the lines of the theory of Kruis & Kusters (1997),

which attempted to reconcile this issue by marrying the concept of Yuu (1984) for the small *St* case and that of Williams & Crane (1983) (which does not consider shear-driven collisions) for the large *St* case, to bubble–particle collisions (see Appendix A). The original formulation of Kruis & Kusters (1997) accounted for collisions of particles of equal density only. We further note the work of Fayed & Ragab (2013), who employed the model of Zaichik, Simonin & Alipchenkov (2010), which was developed originally for collisions between particles with arbitrary but equal density assuming a joint-normal fluid–particle velocity distribution, to the bubble–particle case. Recently, Kostoglou *et al.* (2020*a*) proposed another model that is specific to the case of very fine particles that essentially follow the flow, such that the relative velocity is dominated by the bubble slip velocity.

A common feature of almost all these models is that they are direct adaptations of concepts developed for collisions between heavy particles. They therefore fail to account for fundamental differences in how bubbles and heavy particles react to a turbulent flow. Most strikingly, for example, the response to fluid accelerations given in (2.9) is in opposite directions as β switches sign from negative to positive from $\rho_i > \rho_f$ to $\rho_i < \rho_f$. Similarly, applying the centrifuge picture to light particles such as bubbles, one expects them to concentrate in regions of high vorticity as they travel to the centre of the eddies. This implies that heavy and light particles segregate in a turbulent flow, as has indeed been observed (Calzavarini *et al.* 2008*a*; Fayed & Ragab 2013). As a consequence, it is expected that $g_{bp}(r_c) < 1$ in these cases, such that preferential concentration is expected to lead to a decrease in $\Gamma_{bp}^{(STc)}$ for collisions between heavy and light particles. Such aspects cannot be quantified easily from laboratory-scale flotation set-ups (e.g. Darabi *et al.* 2019) since it is difficult to disentangle the many factors influencing the overall flotation rate. Numerically, Wan *et al.* (2020) observed no reduction of the RDF, but increased relative velocities for bubble–particle pairs based on a point-particle simulation while taking gravitational effects into account. For cases without gravity, Fayed & Ragab (2013) reported $g_{bp}(r_c) < 1$ and relative velocities matching those predicted by the theory of Zaichik *et al.* (2010) for simulations of the extreme case $\rho_b/\rho_f = 0$ and $\rho_p/\rho_f \to \infty$ across a range of τ_i. It is the goal of the present study to add to this a systematic investigation of how bubble–particle relative behaviour affects their collision statistics in the low- to moderate-*St* regime, and to assess how this affects modelling outcomes.

3. Methods

3.1. *Fluid phase*

To obtain the background turbulence, we solve the Navier–Stokes equation and the continuity equation for incompressible flow:

$$\frac{\mathrm{D}\boldsymbol{u}}{\mathrm{D}t} = -\frac{1}{\rho_f}\,\nabla P + \nu\,\nabla^2\boldsymbol{u} + \boldsymbol{f}_\Psi, \tag{3.1a}$$

$$\nabla \cdot \boldsymbol{u} = 0, \tag{3.1b}$$

where $\mathrm{D}/\mathrm{D}t$ is the material derivative following a fluid element, t is the time, and P is the pressure. The forcing $\boldsymbol{f}_\Psi$, which is non-zero only for the wavenumbers $|\kappa|/|\kappa_0| < 2.3$ (i.e. the largest scales), with $|\kappa_0|$ being the smallest wavenumber along each direction, is added to counter dissipation and maintain statistical stationarity. We employ the widely used Eswaran & Pope (1988) forcing scheme (Chouippe & Uhlmann 2015; Spandan *et al.* 2020). In brief, a complex vector is generated in Fourier space for the forced wavenumbers

Re_λ	$\mathcal{N}$	$\bar{\varepsilon}$	η	$k_{max}\eta$	u_η	u'/u_η	u'_x/u'_y	T_L/τ_η	$N_{b,p}$
72	256^3	58.0	0.0041	3.3	0.62	4.3	0.98	19	10 000
175	512^3	349	0.0013	2.1	0.77	6.6	0.97	43	77 700–140 000

Table 1. Statistics of the homogeneous isotropic turbulence: the grid size ($\mathcal{N}$), pseudo-dissipation ($\bar{\varepsilon}$), Kolmogorov length scale (η), maximum wavenumber (k_{max}), Kolmogorov velocity (u_η) scale, r.m.s. velocity fluctuations (u'), large-scale isotropy (u'_x/u'_y), and large eddy turnover time (T_L) relative to the Kolmogorov time scale (τ_η). Here, N_b, N_p are the numbers of bubbles and particles, respectively.

by multiple Uhlenbeck–Ornstein processes. This vector is then projected onto the plane normal to the wavevector, thereby ensuring that $\boldsymbol{f}_\psi$ is divergence-free. To simulate the fluid motion, a second-order finite-difference solver is implemented on a staggered grid (Verzicco & Orlandi 1996; van der Poel *et al.* 2015). All spatial derivatives, including the nonlinear terms, are discretised by a second-order central finite-difference method. The simulation domain is a cubic box with length $L_{box} = 1$ and triply periodic boundary conditions to eliminate boundary effects. Time marching is performed using a fractional step third-order low-storage Runge–Kutta scheme and the implicit Crank–Nicolson scheme for all viscous terms at a maximum Courant–Friedrichs–Lewy (CFL) number 1.2. The CFL number is $\max(|u_1| + |u_2| + |u_3|)\,\Delta t/\Delta x$ over all cells, where the grid spacing Δx is identical in all the three dimensions. Here, u_1, u_2, u_3 are the x-, y-, z-components of $\boldsymbol{u}$, and Δt is the time step. The simulation is parallelised via slab decomposition along the z-direction.

Turbulence with $Re_\lambda = 72$ and 175 is generated from an initially quiescent fluid following the tuning method proposed by Chouippe & Uhlmann (2015). The simulations are allowed to run until the pseudo-dissipation $\bar{\varepsilon}$ and Re_λ are statistically stationary over at least $30T_L$. These statistically stationary flow fields are then used as the starting fields for the point-particle simulations. The flow statistics are listed in table 1. For validation, the longitudinal and transverse energy spectra are plotted in figure 1. Excellent agreement with the literature is shown.

3.2. *Suspended phases*

Bubbles and particles in the system are modelled using the point-particle approximation, where forces act on point masses. The bubble and particle dynamics are governed by (Maxey & Riley 1983; Tchen 1947)

$$\frac{4}{3}\,\pi r_i^3 \rho_i\,\frac{\mathrm{d}\boldsymbol{v}_i}{\mathrm{d}t} = 6\pi\mu r_i f_i(\boldsymbol{u} - \boldsymbol{v}_i) + \frac{4}{3}\,\pi r_i^3 \rho_f\,\frac{\mathrm{D}\boldsymbol{u}}{\mathrm{D}t} + \frac{2}{3}\,\pi r_i^3 \rho_f\left(\frac{\mathrm{D}\boldsymbol{u}}{\mathrm{D}t} - \frac{\mathrm{d}\boldsymbol{v}_i}{\mathrm{d}t}\right), \qquad (3.2)$$

where $\mu = \nu\rho_f$ is the absolute viscosity, r_i is determined from St_i, and $\boldsymbol{u}$ is evaluated at particle position in this equation. The three terms on the right-hand side of (3.2) are the drag force, the pressure gradient force and the added mass force, respectively. Note that history forces, lift and reverse coupling are not considered to render it easier to disentangle the relative behaviour of bubble and particles. Nevertheless, as the lift force can be expected to play a role for bubbles, its effect will be discussed in § 4.3. Furthermore, a one-way coupled system is a consistent choice to study the geometric collision rate where hydrodynamic interactions are neglected. It entails the assumption of the dilute limit in which turbulence modifications by the suspended species are negligible (Brandt
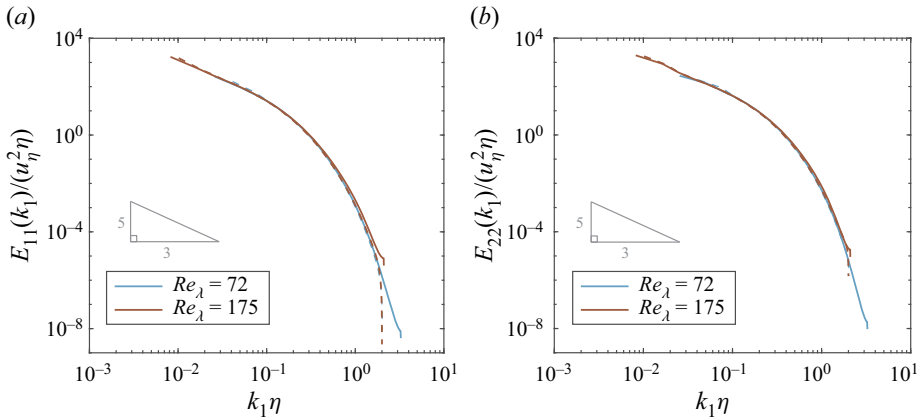
959 A6-8

Figure 1. The (*a*) longitudinal and (*b*) transverse energy spectra in single-phase statistically stationary homogeneous isotropic turbulence. Dashed lines show the data from Jiménez *et al.* (1993); triangles represent the $-5/3$ power law. The agreement with the literature is excellent, so the dashed lines can be obscured, especially in (*b*).

& Coletti 2022). The correction factor $f_i = 1 + 0.169\,Re_i^{2/3}$ accounts for finite bubble or particle Reynolds number $Re_i = 2r_i\,|\boldsymbol{w}_i|/\nu$, and implies the assumption of rigid spheres that obey the no-slip boundary condition for both species (Nguyen & Schulze 2004). This is realistic since liquids in flotation cells typically contain significant amounts of surfactants, so that the bubble surfaces would likely be contaminated (Nguyen & Schulze 2004; Huang, Legendre & Guiraud 2012). Although other commonly used expressions for f_i are available, the difference is minimal, as shown in Appendix C.

Equation (3.2) is solved for each bubble and particle using a finite-difference scheme. To determine the flow velocities and the velocity gradients at bubble and particle positions, these quantities are interpolated from the Eulerian grid of the fluid solver to the particle positions using tri-cubic Hermite spline interpolation with a stencil of four points per direction. This choice is made as Hermite splines are comparable in accuracy (van Hinsberg, Clercx & Toschi 2017) and computationally cheaper to implement than B-splines (Ostilla-Monico *et al.* 2015). Time marching of $\boldsymbol{v}_i$ is performed with the explicit forward Euler method, and that of the positions of the suspended phases is done using the second-order Adams–Bashforth scheme. For stability, the time step is restricted such that neither the fluid nor the particle CFL number ($\max(v_{i1}, v_{i2}, v_{i3})\,\Delta t/\Delta x$) exceeds the value 1.2. This limit is enforced in both the suspended- and fluid-phase solvers, which run with the same simulation time step. We have compared particle statistics to data from the literature in order to verify our code, and those results are included in Appendix B.

Collisions between particles and bubbles are treated as 'ghost collisions'. Under this approach, a 'collision' occurs once the centres of the members of an approaching pair reach the collision distance and the colliding pair pass each other without interaction. The collision radii are determined through the virtual radii r_i as computed from St_i. This scheme is often employed by simulations of particles in turbulence (Bec *et al.* 2005, 2007; Goto & Vassilicos 2008; Voßkuhle *et al.* 2014; Ireland *et al.* 2016) and has been shown to be consistent with the formulation of $\Gamma_{pp}^{(ST)}$ (Wang, Wexler & Zhou 1998). To suppress the effect of different length scales when comparing collision pairs, we take $r_c = r_b + r_p$ for every type of collision. This is unlike studies examining solely particle–particle collisions, which define $r_c = 2r_p$ (e.g. Voßkuhle *et al.* 2014; Ireland *et al.* 2016). Numerically, these

collisions are detected with the 'proactive' detection scheme in Sundaram & Collins (1996).

The details of the simulation of the suspended phases are as follows. Particles ($\rho_p/\rho_f = 5$) and bubbles ($\rho_b/\rho_f = 1/1000$) with $St_i = 0.1$–3 were seeded randomly and homogeneously (10 000–140 000 each) into the turbulent flow after it had reached a statistically stationary state as described in § 3.1. The density ratios correspond to sulphide minerals colliding with air bubbles in water, while the simulated St range falls within $0.1 \lesssim St \lesssim 100$, which corresponds to particle sizes yielding the highest mineral recovery rate in conventional flotation cells ($10\,\mu\text{m} \lesssim r_p \lesssim 100\,\mu\text{m}$ when $\nu = 10^{-6}\,\text{m}^2\,\text{s}^{-1}$ and $\varepsilon = 5\,\text{m}^2\,\text{s}^{-3}$, following Ngo-Cong *et al.* 2018). For each case, bubbles and particles have identical St_i to focus on the effect of different densities and to keep the parameter space manageable. The upper limit $St_i \leq 3$ is mandated by the fact that the increasingly large (virtual) bubble radius for larger St violates the point-particle approximation. For $St_b = 3$ and at $Re_\lambda = 175$, we have $r_b/\eta \approx 5$, which is already marginal (Homann & Bec 2010). We monitor the p.d.f.s of bubble and particle positions for statistical stationarity. Once this has been reached, collision statistics are collected over at least $7.7T_L$. Two kinds of statistics are evaluated: in a fixed reference frame considering all particles/bubbles (Eulerian statistics), and along individual trajectories of the pairs that collide (Lagrangian statistics). The former are computed at least every $\sim 0.06T_L$, while the latter are calculated every time step (with only 25 % of all bubbles for the bubble–bubble case as the number of colliding bubbles is high). All the statistics presented are time- and ensemble-averaged unless indicated otherwise.

4. Results

4.1. *Eulerian statistics*

4.1.1. *Collision kernel*

Figure 2(*a*) shows simulation results for the dimensionless bubble–particle (bp), bubble–bubble (bb) and particle–particle (pp) collision kernels Γ. In addition to determining Γ based on counting the number of collisions per time step (solid triangles), the collision kernels for $Re_\lambda = 175$ are determined indirectly via the RDF and the effective radial collision velocity according to (1.2) (shown as dots). Both results match closely, verifying our analysis procedure. With the normalisation by τ_η/r_c^3 suggested by the Saffman–Turner framework, the results are insensitive to the change in Re_λ for the pp and bp cases, but not for bb collisions. From the data, it is further evident that the relative behaviour of bubbles and particles is distinct from that of identical particles. For collisions between identical species, $\Gamma\tau_\eta/r_c^3$ is maximum when $St \sim 1$, while $\Gamma_{bp}\tau_\eta/r_c^3$ exhibits a minimum for this value of St. This trend is not captured by any of the models for the bp case discussed in § 2.4, for which the predictions are included as lines in figure 2(*a*). Generally, the model predictions are also significantly higher than the actual collision rates obtained from the simulations, the exception being the Saffman & Turner (1956) model, which best captures the magnitude yet fails to predict the proper St-trend, as is illustrated more clearly in figure 2(*b*).

The fact that the Abrahamson (1975) and large-St Kruis & Kusters (1997) predictions do not match the data is to be expected as the present St range does not match the assumptions made in these frameworks. Naturally, this also transfers to all approaches based on $\Gamma_{bp}^{(A)}$, and the somewhat better agreement with our data for models employing (2.7) and (2.8) instead of (2.6) is rather an artefact of the inconsistencies discussed earlier.
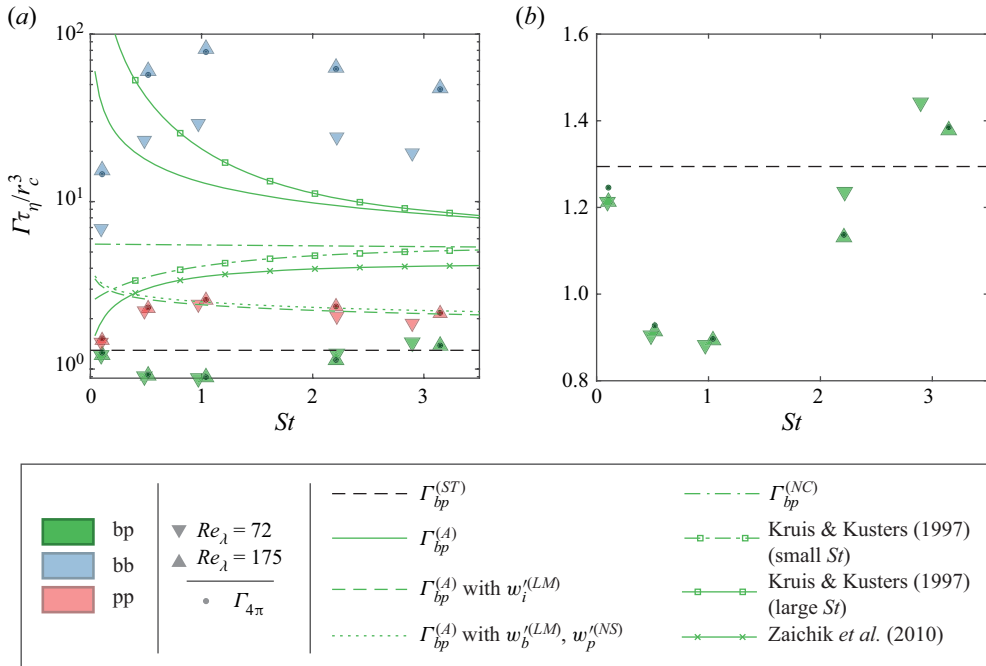
Figure 2. (*a*) The dimensionless bubble–particle (bp), bubble–bubble (bb) and particle–particle (pp) collision kernels at collision distance. The triangle symbols denote Γ determined directly from the collision rate, while $\Gamma_{4\pi}$ (shown only for the $Re_\lambda = 175$ cases) is calculated according to (1.2). Unless specified otherwise, the colour conventions for all figures follow this figure. (*b*) Zoomed-in version of (*a*) plotted on linear scale.

This is emphasised by figure 3(*a*), where the large difference between the modelled slip velocities and the mean-square bubble/particle velocities $v_i'^2$ is obvious. Notably from the same figure, $v_p'^2$ is well predicted by the models of Abrahamson (1975), Kruis & Kusters (1997) (small *St*) and Zaichik *et al.* (2010). On the other hand, model estimates for $v_b'^2$ are generally too high. It is insightful to note the stark overprediction by (2.6) as the underlying framework by Abrahamson (1975) is also employed in the models by Ngo-Cong *et al.* (2018). The resulting overprediction of $v_b'^2$ might therefore explain in part why the estimate of $\Gamma_{bp}^{(NC)}$ is too large even though their concept (which is based on Yuu (1984)) is in principle more suitable for the moderate values of *St* here. Unlike Abrahamson (1975), Kruis & Kusters (1997) (small *St*) include dissipation range scaling in their modelling, which is seen to improve the prediction at $St \lesssim 1$ but still overestimates $v_b'^2$ for larger *St*. Finally, there is another factor, which affects all models. Bubbles especially do not sample the flow randomly, such that the mean-square fluid velocity at bubble locations $\langle u'^2 \rangle_b$ is almost 10 % lower than u'^2, as shown in figure 3(*b*). This implies that bubbles sample flow regions with weaker fluid velocity fluctuations such that using u'^2 as model input may overestimate $v_b'^2$. Figure 3(*b*) also shows that this effect is less pronounced for heavy particles. The underlying cause for these observations is preferential sampling of flow regions, which we will discuss in § 4.1.2.

4.1.2. *Bubble/particle spatial distribution*
In order to elucidate in particular the *St* trends for Γ_{bp}, we first investigate the distribution of bubbles and particles in the flow. While all the models assume homogeneous
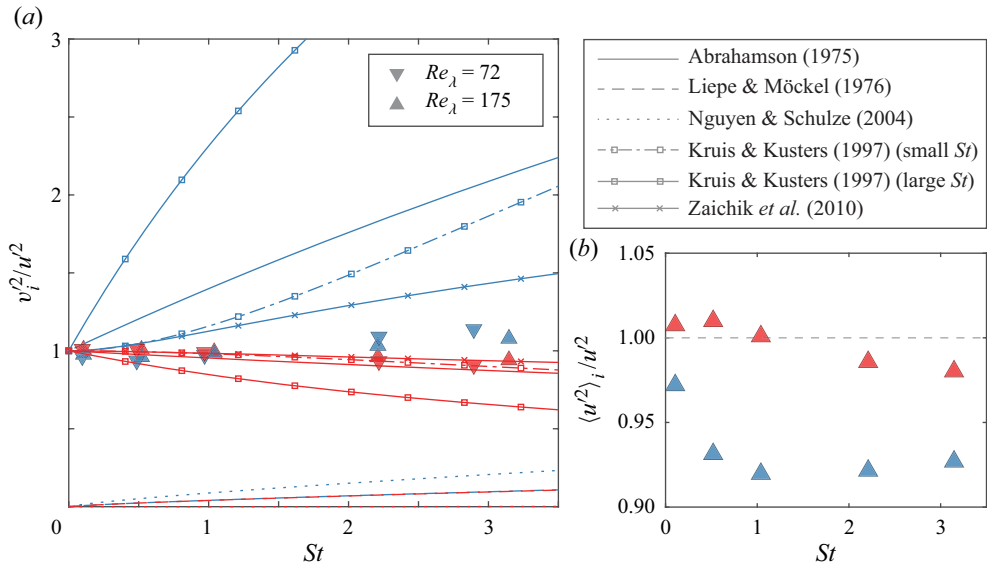
Figure 3. (*a*) The mean-square velocity of bubbles and particles at various *St*. Models are shown for $Re_\lambda = 175$ only. (*b*) The mean-square fluid velocity conditioned at bubble/particle positions for $Re_\lambda = 175$.

distributions, this does not hold at intermediate *St*, as figure 4 confirms, where instantaneous snapshots of the bubble and particle fields at different *St* and $Re_\lambda = 175$ are shown. For $St = 1$ and 3, bubbles and particles are seen to cluster but do so in different regions of the flow. This behaviour has been observed previously in the literature (Calzavarini *et al.* 2008*a*; Fayed & Ragab 2013; Wan *et al.* 2020) and is additionally shown by the different mean-square fluid velocity at bubble/particle positions in figure 3(*b*). To investigate this preferential concentration, we plot the norm of the rotation $\langle R^2 \rangle_r$ and strain $\langle S^2 \rangle_r$ rates of the flow at the particle/bubble positions in figure 5, with $\langle \cdot \rangle_r$ denoting an ensemble average over particles in pairs with separations smaller than *r*. For tracers ($St = 0$), we obtain $\tau_\eta^2 \langle R^2 \rangle_r = \tau_\eta^2 \langle S^2 \rangle_r = 0.5$ with $r \to \infty$, consistent with the analytical result in statistically stationary homogeneous isotropic turbulence. For the other cases, $\langle R^2 \rangle_r$ and $\langle S^2 \rangle_r$ are conditioned on pairs with $r \leq 2r_c$. Figure 5(*a*) shows that bubbles (particles) cluster in regions of high (low) rotation rate, which is consistent with the centrifuge picture. Due to the clustering, conditioning has little effect for monodisperse collisions, and the results are therefore very close to single particle statistics. This is different for bp pairs, where R^2 is consistently lower (higher) for bubbles (particles) close to a particle (bubble). These observations imply that bp collisions occur for a subset of bubbles/particles that is located outside of their respective 'preferred' location within the flow. We note that correlations between particle/bubble locations and the strain rate (figure 5*b*) are much weaker and do not display the same qualitative trends observed for R^2. This is consistent with observations by e.g. Ireland *et al.* (2016) and Wang *et al.* (2020), who also found only a weak correlation between the positions of heavy particles and regions of the flow with low strain rate.

A consequence of the preferential concentration in different flow regions is that bubbles and particles become segregated. This effect is quantified by the RDF $g(r)$. Essentially, $g(r)$ relates the actual number of pairs with separation *r* to that expected for uniformly distributed particles. Therefore, $g(r) = 1$ when particles are uniformly distributed, $g(r) > 1$ implies clustering, and $g(r) < 1$ implies segregation (Saw 2008). Figure 6(*a*)
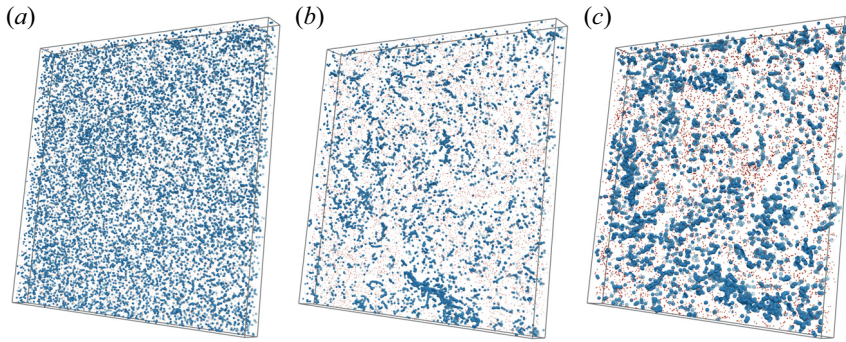
959 A6-12

Figure 4. Instantaneous snapshots of bubbles and particles in a slice with width $\times$ height $\times$ depth $= L_{box} \times L_{box} \times 20\eta$ in the non-transient state for $Re_\lambda = 175$ at (*a*) $St = 0.1$, (*b*) $St = 1$, and (*c*) $St = 3$. The size of the $St = 0.1$ bubbles and particles is tripled for visibility.
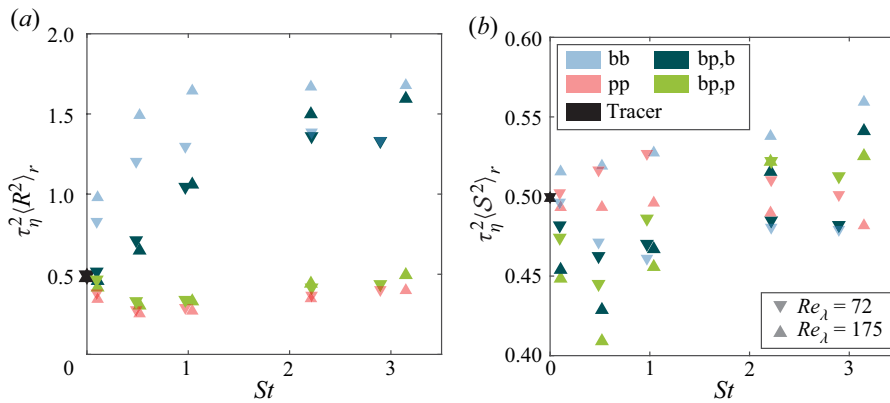

Figure 5. Average value of the norm of (*a*) the rotation rate R^2, and (*b*) the strain rate S^2, of the flow at bubble/particle/tracer positions. The bubble and particle data are conditioned on pairs with separation $r \leq 2r_c$. Here, bp,b (bp,p) refer to bubbles (particles) in bubble–particle pairs.

shows results for the RDF at collision distance from our simulations. Bubble–particle pairs indeed segregate, and the segregation is strongest when $St = 1$, as reflected by the local minimum of $g(r_c)$. This is compatible with the corresponding behaviour of bubbles and particles, which always cluster for the tested parameters, with maximum clustering when $St \sim 1$. Increasing Re_λ increases segregation slightly, but the effect is weak.

Figure 6(*b*) displays the bubble–particle RDF as a function of r at $Re_\lambda = 175$, which helps us to understand the effect of different length scales. The shape of the $g(r)$ curves is distinctly different from the power-law behaviour reported for the monodisperse case (Ireland *et al.* 2016). For all St, there is an essentially flat region for $g(r)$ at small scales, followed by a transition region with the steepest gradient at intermediate scale $\sim 10\eta$ before approaching 1 for large separations. This behaviour suggests that the relevant length scale for the segregation, i.e. a typical distance between bubble and particle clusters, is at intermediate scales. To quantify this more precisely, we define the separation corresponding to the point of inflexion in $g_{bp}(r)$ as the segregation length scale r_{seg}. The values of r_{seg} are marked by crosses in figure 6(*b*), and plotted against St in the inset. The figure shows that r_{seg}/η increases approximately linearly with St and increases slightly with Re_λ. These findings are consistent with those by Calzavarini *et al.* (2008*a*),
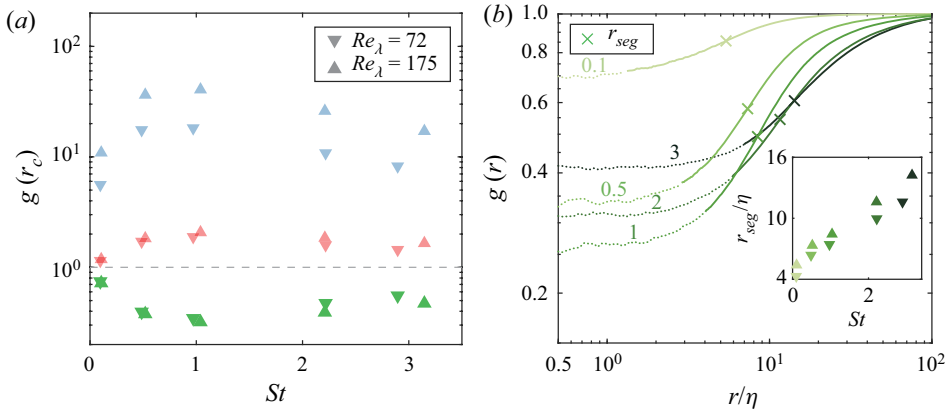
Figure 6. (*a*) RDF at collision distance. (*b*) The bubble–particle RDF as a function of *r* and the segregation length scale r_{seg} at $Re_\lambda = 175$. The number above each line is the corresponding *St*, and the dotted segments denote the RDF below the collision distance. Inset shows r_{seg} at various *St*.

who studied segregation based on a concept inspired by Kolmogorov's distance measure (Kolmogorov 1963). In particular, these authors also report segregation scales $\sim 10\eta$ with an increasing trend for higher Re_λ.

The trends observed for $g(r_c)$ in figure 6(*a*) remarkably resemble those discussed for the *St* dependence of Γ earlier, in the context of figure 2. It is therefore suggestive to think that the effects of segregation may explain in particular the discrepancy between the data and $\Gamma^{(ST)}$. We can check this by plotting $\Gamma^{(STc)}$ as defined in (2.2), which is shown as hollow symbols in figure 7(*a*). From this plot, it can be seen that correcting $\Gamma^{(ST)}$ with the RDF leads to an almost perfect match with the pp collision kernel. This differs from, but is only seemingly at odds with, the results in Voßkuhle *et al.* (2014) due to the larger collision distance considered here as a consequence of keeping $r_c = r_b + r_p$ constant for all collision types. This therefore implies that while pp collisions at moderate *St* are governed by the sling mechanism at small separations, they remain shear-dominated at larger ones. In contrast, $\Gamma^{(STc)}$ overcorrects the bp collision kernel and undercorrects that of bb collisions. In figure 7(*b*), we replot the same data in the form of the ratio $\Gamma^{(STc)}/\Gamma$, which can be interpreted as the relative contribution of the shear mechanism (compensated for segregation/clustering) to the overall collision rate. For pp collisions, this ratio is very close to 1 throughout. The situation is different for the bb case, where $\Gamma^{(STc)}/\Gamma$ approaches 1 only for the lowest *St* considered, and the value drops significantly for the higher *St*. Consistently the lowest values for $\Gamma^{(STc)}/\Gamma$ are observed for bp collisions where the value quickly drops to around 0.5, which implies that a significant part of the relative velocities cannot be explained by the shear mechanism in this case. It is important to stress here that keeping r_c constant for all collision types for a given *St* removes this as a factor, such that the observed trends across species can only be rooted in differences in the relative approach velocities, which will be studied next.

4.1.3. *Relative velocities*

We show results for the non-dimensional effective radial approach velocity S_-/u_η at collision distance in figure 8(*a*). The non-dimensional approach velocity increases with *St* and also slightly with Re_λ for collisions involving bubbles, whereas it has only a very
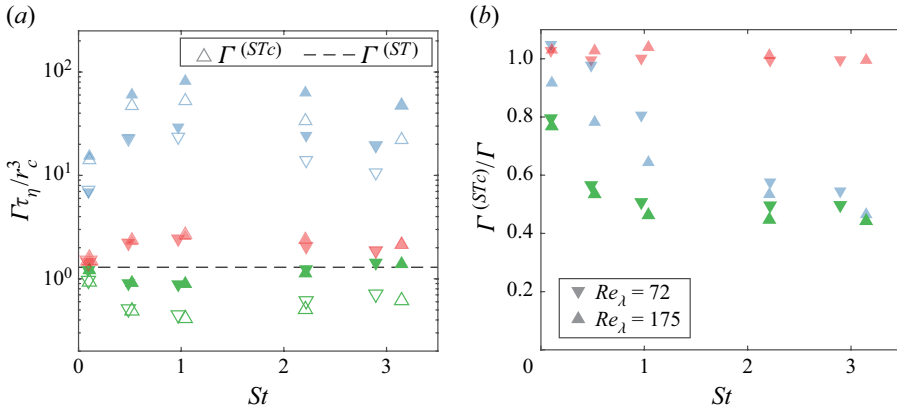
Figure 7. (*a*) The dimensionless collision kernel (solid symbols) and the Saffman–Turner prediction after accounting for the RDF $\Gamma^{(STc)}$ (hollow symbols). (*b*) The ratio between $\Gamma^{(STc)}$ and the collision kernel.
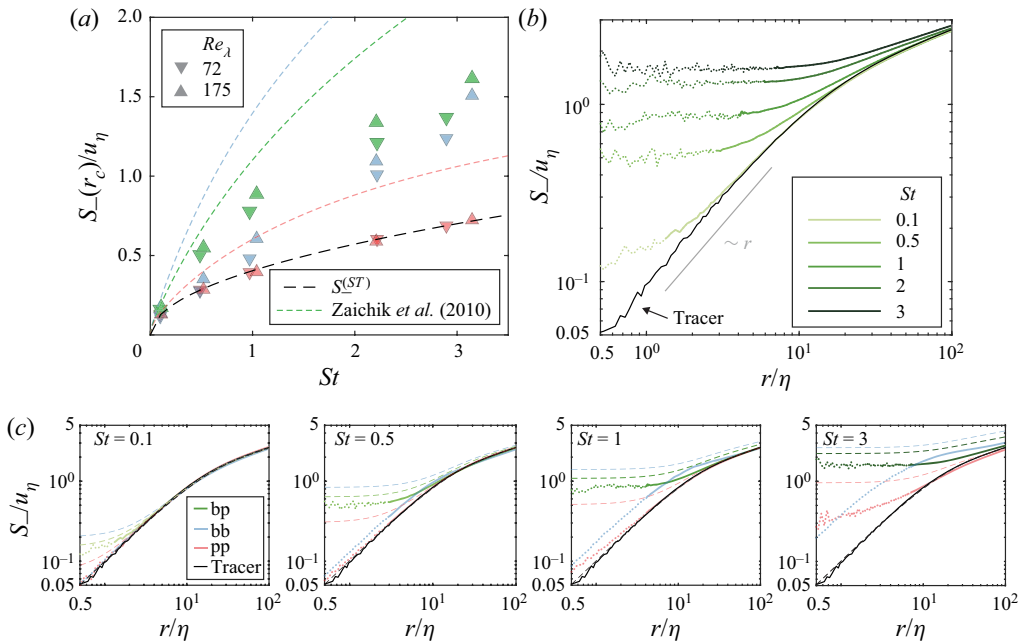

Figure 8. (*a*) The effective radial collision velocity. (*b*) The effective bubble–particle radial approach velocity against pair separation r at $Re_\lambda = 175$. (*c*) The effective radial approach velocity of each type of collisions across $St = 0.1$ to $St = 3$ at $Re_\lambda = 175$. The dashed lines show the prediction by Zaichik *et al.* (2010).

weak Re_λ dependence for pp collisions, as also reported in Ireland *et al.* (2016). Consistent with figure 7, the approach velocities are highest for bp collisions and lowest in the pp case.

To understand these trends, it is instructive to consider S_- as a function of r, which is presented in figure 8(*b*) for bp collisions for different St, and in the plots of figure 8(*c*) for different collision types at constant St. Also shown in these figures is the effective approach velocity for tracer particles, for which S_- is proportional to r in the dissipation range, as expected. In particular, for low St, where $S_-(r)$ remains close to the tracer
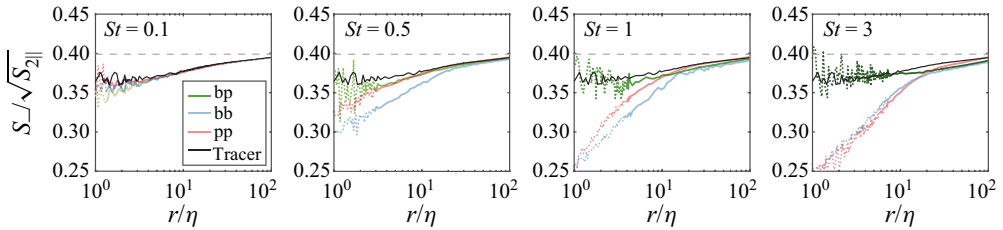
Figure 9. The ratio of the effective radial approach velocity to the standard deviation of the radial component of the relative velocity Δv_r at $Re_\lambda = 175$.

curve, this in part explains the St dependence of $S_-(r_c)$ as r_c increases with increasing St. However, the curves also 'peel off' the linear scaling at increasingly larger distances and to a larger extent as St increases. For the pp case, this is a well-known manifestation of the 'sling effect', where due to path history effects, particles arrive at the same location with different velocities such that their relative velocities exceed those of the fluid. Note that while the bb case has a larger S_- than the tracer case, the linear scaling remains mostly unchanged there, such that the difference presumably is rather due to preferential concentration effects and the fact that the slip velocity at the same St is higher for this case (see (2.9)). The deviations from the tracer behaviour are strongest for the bp case throughout, and already for $St \geq 2$ S_- are essentially independent of r for $r \gtrsim 10\eta$. The decorrelation between bubble and particle velocities implicit in these observations is the reason why S_- is largest for all St in figure 8(a). The model of Zaichik *et al.* (2010) fails to reproduce this feature. Instead, S_- from the model is highest for bb collisions, such that the trend falls in line with that of $v_i'^2$ (see figure 3). Plotting the model prediction against the separation distance in figure 8(c) confirms that this trend persists over all r. Approach velocities are also generally overpredicted by the model, which is in part also related to the differences observed for $v_b'^2$ in figure 3 and to the significant peel off the linear scaling especially for the bb case. Consistent with the results in figure 7, S_-^{pp} at both Re_λ is matched very well by the Saffman–Turner model $S_-^{(ST)} = 0.5r_c\sqrt{2\varepsilon/15\nu\pi}$, where the prefactor 0.5 accounts for the fact that only separating pairs are considered here.

In modelling approaches (e.g. Abrahamson 1975; Yuu 1984; Kruis & Kusters 1997; Zaichik *et al.* 2010; Ngo-Cong *et al.* 2018), it is common to deduce S_- based on a Gaussian distribution of the relative radial velocity Δv_r. In this case, the ratio $S_-/\sqrt{S_{2\parallel}}$ can be determined to be $1/\sqrt{2\pi} \approx 0.4$, where the variance is defined as

$$S_{2\parallel}(r) = \int_{-\infty}^{\infty} (\Delta v_r)^2 \text{p.d.f.}(\Delta v_r | r) \, \text{d}(\Delta v_r). \tag{4.1}$$

It was already reported in Ireland *et al.* (2016) that $S_-/\sqrt{S_{2\parallel}}$ can drop significantly below the Gaussian value for pp collisions at $St \sim 1$ and for small r_c. This is confirmed by our results in figure 9, where also the bb case is seen to follow similar trends. For bp collisions, the ratio remains much closer to the Gaussian value, almost indifferent to St and close to the tracer result. Relative velocities are therefore better approximated by the Gaussian assumption for the bp case, while the overprediction of S_- resulting from doing so is larger for the monodisperse collisions.

For a more quantitative investigation of variation of S_- across collision types, we plot the excess bubble–particle effective radial collision velocity $\Delta S_- = S_-^{bp} - (S_-^{bb} + S_-^{pp})/2$ in figure 10(a). At small St, such an additional approach velocity arises for the bp case from the fact that, due to the change in sign of β_i in (2.9), bubbles and particles react differently
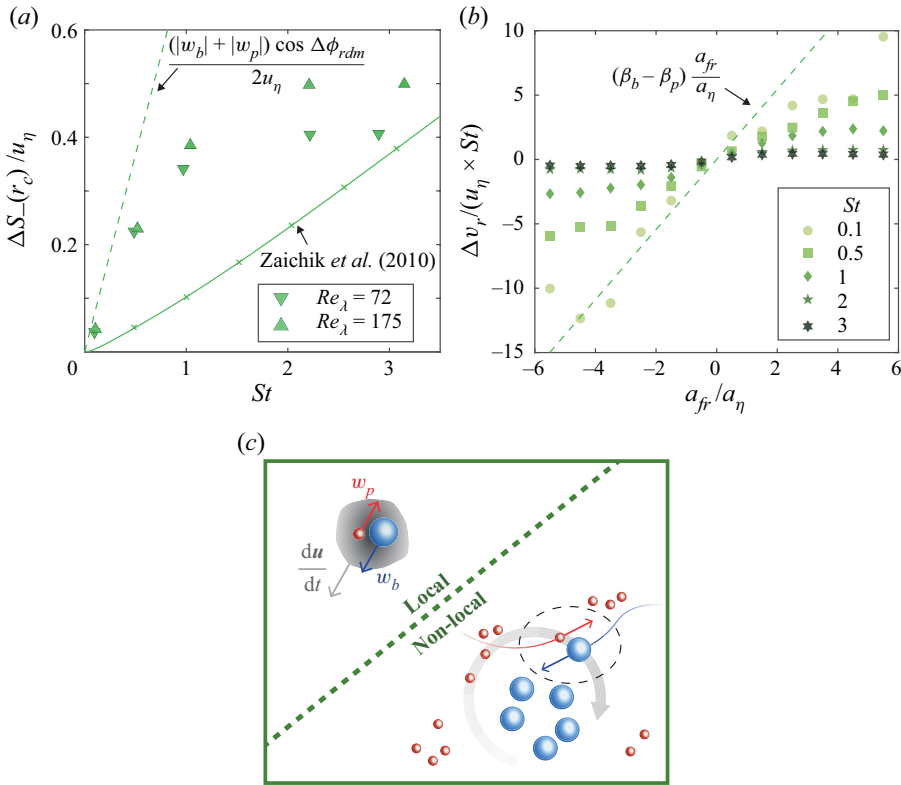
959 A6-16

Figure 10. (*a*) The excess bubble–particle effective radial collision velocity $\Delta S_- = S_-^{bp} - (S_-^{bb} + S_-^{pp})/2$ from simulations over a range of *St*. The factor $1/2$ for the dashed line accounts for the fact that S_- is obtained by averaging only over the negative portion of p.d.f.$(\Delta v_r | r_c)$ as defined in (1.3). (*b*) The radial component of the relative velocity conditioned on pairs with $r \in [r_c - \eta/2, r_c + \eta/2]$ binned by the local radial fluid acceleration at $Re_\lambda = 175$. (*c*) Schematic illustrations of the local and non-local turnstile mechanisms.

when subjected to the same fluid acceleration. Indeed, figure 10(*b*) shows that Δv_r^{bp} conditioned on pairs with $r \in [r_c - \eta/2, r_c + \eta/2]$ at small *St* closely follows the resulting expression for the relative velocity $\Delta v_r / u_\eta = St\,(\beta_b - \beta_p) a_{fr}/a_\eta$, where a_{fr} is the average radial fluid acceleration at bubble and particle positions. We therefore conceptualise the resulting excess bp collision velocity as the local 'turnstile mechanism', since bubbles and particles respectively move in opposite directions, as illustrated in figure 10(*c*). An estimate for this effect can be obtained using $a_f \sim a_\eta$ in (2.9) and assuming a random orientation between the particle separation vector and the fluid acceleration, resulting in an average angle $\phi_{rdm} = 1\,\mathrm{rad} \approx 57°$. This is shown by the dashed line in figure 10(*a*). While not strictly a prediction for ΔS_-, this estimate is largely consistent with the data for $St < 1$, suggesting that the enhanced approach velocity in this range is indeed due to the local turnstile effect. This is further consistent with the fact that for $St \geq 1$, the correlation of Δv_r^{bp} with the local fluid acceleration is seen to vanish almost completely in figure 10(*b*). A positive ΔS_- is also predicted by the model of Zaichik *et al.* (2010), but underestimates the value in the low-*St* regime. Beyond $St = 1$, ΔS_- flattens off at high values. Along with the observations made in figure 8(*c*), this suggests that the 'path history' effect active at these *St* values is enhanced for the bp case. We can rationalise this in terms of a non-local 'turnstile mechanism' (see figure 10*c*), where differences in the particle velocities arise
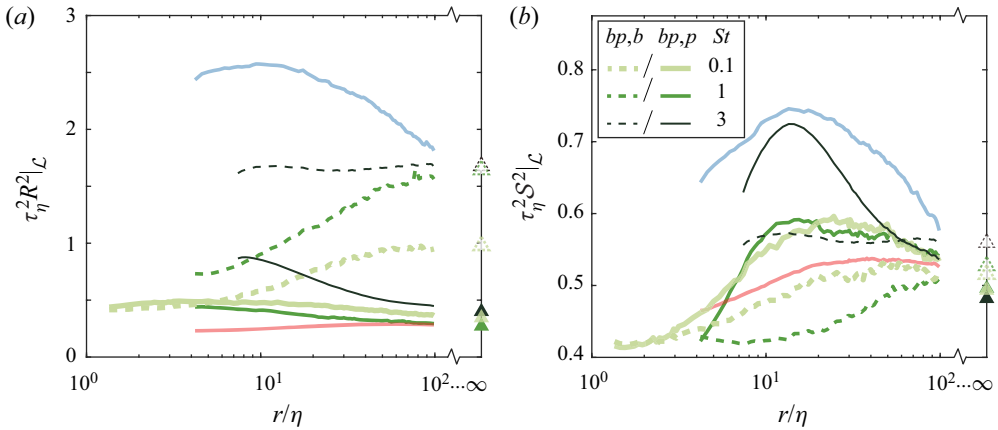
Figure 11. Norm of (*a*) the rotation rates and (*b*) the strain rates of the flow at bubble and particle positions against pair separation conditioned on colliding pairs at $Re_\lambda = 175$ for $r \geq r_c$. Only the $St = 1$ case is shown for bubble–bubble and particle–particle pairs. Also plotted at $r \to +\infty$ is the unconditioned R^2 and $\mathcal{S}^2$ at the respective St.

as bubbles and particles interact differently with larger and more energetic eddies in the flow. As a consequence, their local velocities differ more than for monodisperse cases at equal St. Both the local and non-local inertial effects discussed here enhance the relative approach velocity and therefore explain why $\Gamma_{bp}^{(STc)} < \Gamma_{bp}$ as observed before.

4.2. *Lagrangian statistics*

To better examine the collision process, we adopt the Lagrangian point of view, where colliding pairs are tracked individually for separations $r \leq 100\eta$ up to collision. The corresponding statistics averaging over all pairs with the same r are denoted by the suffix $\mathcal{L}$.

In figure 11, we show how $R^2|_{\mathcal{L}}$ and $\mathcal{S}^2|_{\mathcal{L}}$ vary as functions of r for the colliding pairs. Consistent with the results in figure 5, variations are significantly stronger for $R^2|_{\mathcal{L}}$ (figure 11*a*) compared to $\mathcal{S}^2|_{\mathcal{L}}$ (figure 11*b*). In contrast to the monodisperse case, bubbles and particles need to leave their preferred flow regions in order to collide. While at $r/\eta \sim 100$ the unconditioned preferential concentration (indicated by the symbols in figure 11) is mostly recovered, a pronounced drift generally sets in for $r/\eta \lessapprox 50$. This might suggest that interaction with eddies at this intermediate range plays a role in bringing bubbles and particles together from their segregated locations. At $St = 0.1$, bubbles and particles appear to occupy similar flow regions for $r/\eta \lessapprox 10$ before colliding, i.e. in particular, the $R^2|_{\mathcal{L}}$ curve flattens at these scales, whereas the same is not the case at $St = 1$ and $St = 3$, where the collision distance is larger. These observations are consistent with the considerations regarding the local and non-local turnstile mechanisms made above. It is noteworthy that $R^2|_{\mathcal{L}}$ at $St \leq 1$ varies mostly for bubbles as they approach particles, while at $St = 3$, $R^2|_{\mathcal{L}}$ is almost constant for the bubbles but varies more for the particles. The latter case also stands out in the $\mathcal{S}^2|_{\mathcal{L}}$ plot as the slight decrease in strain values towards collision is not observed there.

In figure 12, we present velocity statistics conditioned on the colliding pairs. In particular, we consider the approach velocity $S_-|_{\mathcal{L}}$ (figure 12*a*) as well as the r.m.s. relative speed $(\Delta v)'|_{\mathcal{L}}$ (figure 12*b*). The approach velocities differ slightly in magnitude from the
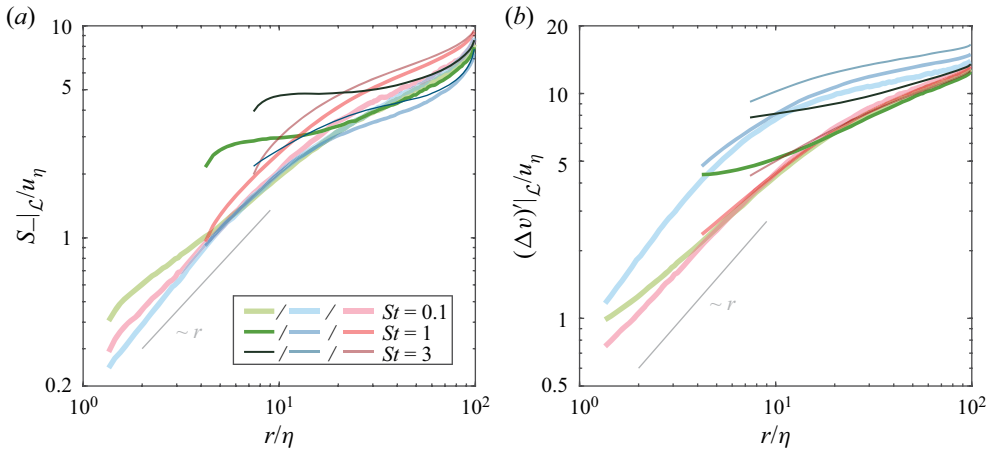
959 A6-18

Figure 12. (*a*) The effective approach velocity, and (*b*) the r.m.s. relative speed, conditioned on colliding pairs at $Re_\lambda = 175$.

unconditioned results in figure 8, but the trends remain consistent. In particular, $S_-^{bp}|_{\mathcal{L}}$ is again largest for separations close to the respective collision distances for all St shown. This is remarkable in view of the fact that $(\Delta v)'|_{\mathcal{L}}$ is actually largest for the bb case. This implies that Δv and r tend to be more anti-aligned for the bp case to yield the higher relative approach velocity.

To measure this, the angle between the separation vector and the relative velocity vector $\Delta\phi$ (see the inset of figure 13*a*) is used. For a head-on approach, $\Delta\phi = 0°$, while $\Delta\phi = 90°$ means that the other particle is circling around in the rest frame of the collision partner. Note that as colliding particles must be approaching each other, $0° \leq \Delta\phi < 90°$. As demonstrated in figure 13(*a*), the bubble–particle pairs are indeed the most anti-aligned, i.e. $\Delta\phi|_{\mathcal{L}}$ is lowest, relative to the other types of collisions near r_c. Figure 13(*b*) shows the ratio of the cosines of $\Delta\phi|_{\mathcal{L}}(r_c)$ as a measure for how much differences in alignment lead to a relative enhancement of $S_-(r_c)$. The ratio is up to 10 for bp relative to bb collisions, and up to $\sim$1.5 compared to particle–particle collisions, and values for both cases are slightly higher at the higher Re_λ. When interpreting the smaller difference between pp and bp collisions here, it should be kept in mind that based on the discussion around figure 7, the collision mechanism differs between these two cases: whereas pp collisions appear predominantly shear-driven, where a good alignment may be expected, inertial effects, for which this is not necessarily the case, play a much more significant role for bp collisions.

4.3. *Effect of lift, finite particle density and nonlinear drag*

Our simulations are performed without the lift force using a finite particle density $\rho_p/\rho_f = 5$ and a nonlinear drag law with $f_i = 1 + 0.169\,Re_i^{2/3}$. To test how sensitive our results are to these parameters, we ran addition simulations for $Re_\lambda = 175$ changing one parameter at a time: adding the lift force $\boldsymbol{F}_L = -2/3\rho_f\pi r_i^3(\boldsymbol{v}_i - \boldsymbol{u}) \times (\nabla \times \boldsymbol{u})$ to the right-hand side of (3.2), setting $\rho_p/\rho_f = \infty$, or using Stokes drag ($f_i = 1$) for both phases. For all of these simulations, r_c is chosen to be identical to the case when $\rho_p/\rho_f = 5$. We compare the results for Γ in figure 14, and those for $g(r_c)$ and $S_-(r_c)$ in figure 15. The plots show that the collision statistics are not sensitive to the lift force. Also more generally, the effect of the lift force is limited, with the most noticeable change occurring
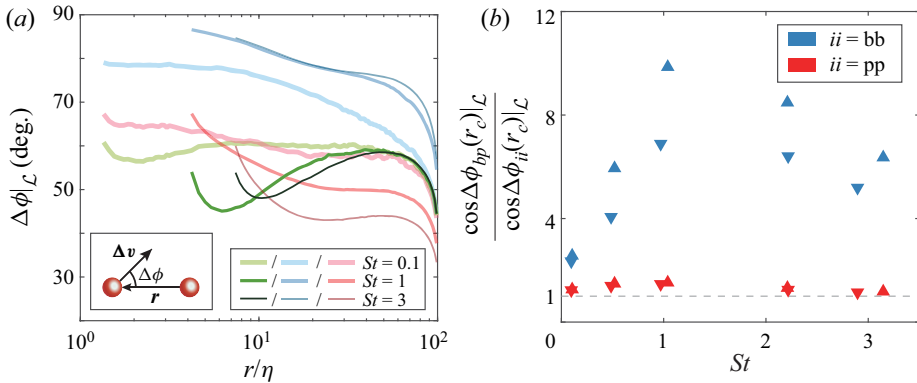
Figure 13. (*a*) The angle between the separation and relative velocity vectors $\Delta\phi$ for $r \geq r_c$ at $Re_\lambda = 175$. Bubble–particle/bubble–bubble/particle–particle pairs are represented by green/blue/red lines as in figure 12. The inset shows the definition of $\Delta\phi$ in the rest frame of the particle on the right. (*b*) The extra angular contribution to the radial component of the bubble–particle collision velocity relative to the bubble–bubble and particle–particle cases.
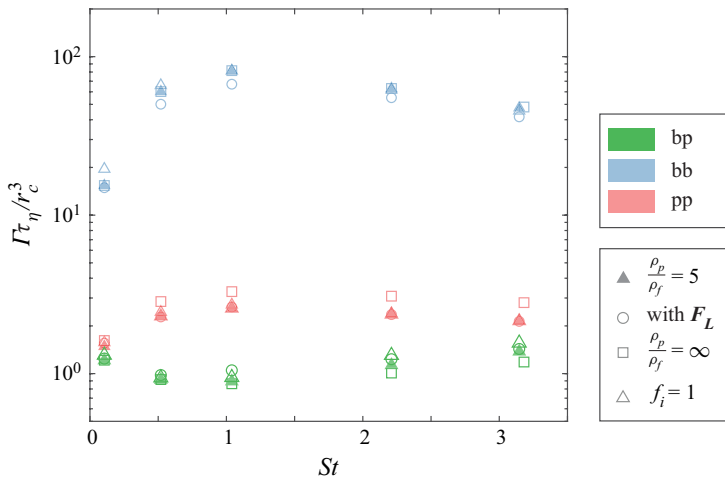

Figure 14. The dimensionless collision kernel for different particle densities simulated, with the lift force included and for the case when the drag correction factor is $f_i = 1$.

for the preferential sampling where we observed a slight decrease in $\tau_\eta \langle R^2 \rangle_r$ at bubble clusters, consistent with Mazzitelli, Lohse & Toschi (2003). It is also evident that the particle density affects these quantities only marginally. Similarly, the results remain largely unchanged for the $f_i = 1$ case, with the exception of a slight increase in Γ_{bp} due to a higher S_- at the larger St. We furthermore note that other expressions for f_i have been proposed in the literature (Schiller & Naumann 1933; Clift, Grace & Weber 2005; Wan *et al.* 2020). These are compared in Appendix C, which shows that they do not differ significantly when $Re_i \lesssim 100$. Hence we conclude that our results would not be sensitive to whichever one of these parametrisations is chosen. Based on the findings in this section, it therefore appears appropriate to neglect lift, and to use the simplifications of linear drag and $\rho_p/\rho_f \to \infty$ for simulations and modelling approaches in the present parameter range.
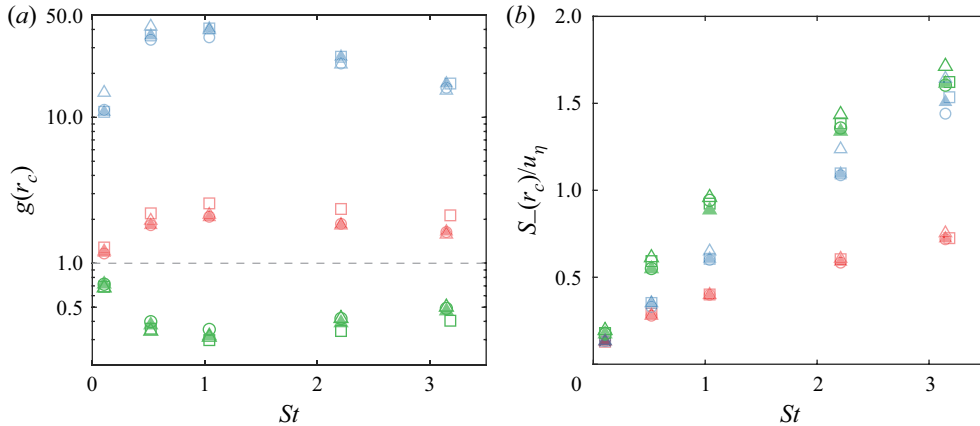
Figure 15. (*a*) The RDF at collision distance, and (*b*) the effective radial collision velocity for different particle densities, with the lift force included and for the case when the drag correction factor is $f_i = 1$. The symbols follow figure 14.

5. Discussion and conclusion

We studied bubble–particle collisions in turbulence using a point-particle approach. Besides a critical appraisal of current models for the problem, our results highlight that the difference in the density ratios between bubbles and particles critically affects the collision statistics. An overview of the physical picture that emerges is presented in figure 16. For $St \to 0$, the shear mechanism is applicable, meaning that the collision velocity is well-described by the local fluid velocity gradient. Once St reaches finite values, bubbles and particles concentrate preferentially in different regions of the flow, which leads to their segregation. This effect reduces the bubble–particle collision kernel Γ_{bp} and is maximal for $St \sim 1$. The correction remains $O(1)$, which is comparable to the enhancement of the collision kernel due to clustering for particle–particle cases, but much less than that for the bubble–bubble cases, respectively. For particle–particle collisions (evaluated at $r_c = r_b + r_p$), the relative approach velocities are found to be entirely consistent with the shear mechanism for the full range of St explored here, such that the collision kernel in these cases is very well approximated by extending the shear-induced collision kernel to account for non-uniform particle concentration $\Gamma^{(STc)}$. The same does not hold for bubble–particle and bubble–bubble collisions, where inertial effects additionally play a role and enhance the effective relative approach velocities beyond the shear scaling. This enhancement is strongest for the bubble–particle case, and we conceptualise this effect in terms of a 'turnstile' mechanism, which is related to the fact that fluid accelerations lead to opposing drift velocities relative to the fluid for bubbles and particles. This happens locally, i.e. on the same fluid element, if St is sufficiently small for bubbles/particles to follow pathlines ($St \leq 0.5$ based on the results in figure 10), but also appears to play a role at higher St, where the path history becomes more relevant. For $St \gtrsim 2$, the ratio $\Gamma^{(STc)}/\Gamma$ and the values of the effective radial approach velocity at contact $S_-(r_c)$ are comparable for bubble–particle and bubble–bubble collisions, which indicates that the 'non-local' turnstile is less prevalent there, in line with the fact that local particle/bubble velocities become increasingly random at larger St.

Our method does not allow us to assess the high St (kinetic-gas-like) regime since bubble sizes violate the point-particle assumption. Applying the Abrahamson (1975) model pertinent to this regime to the present data vastly overpredicts the collision kernel,
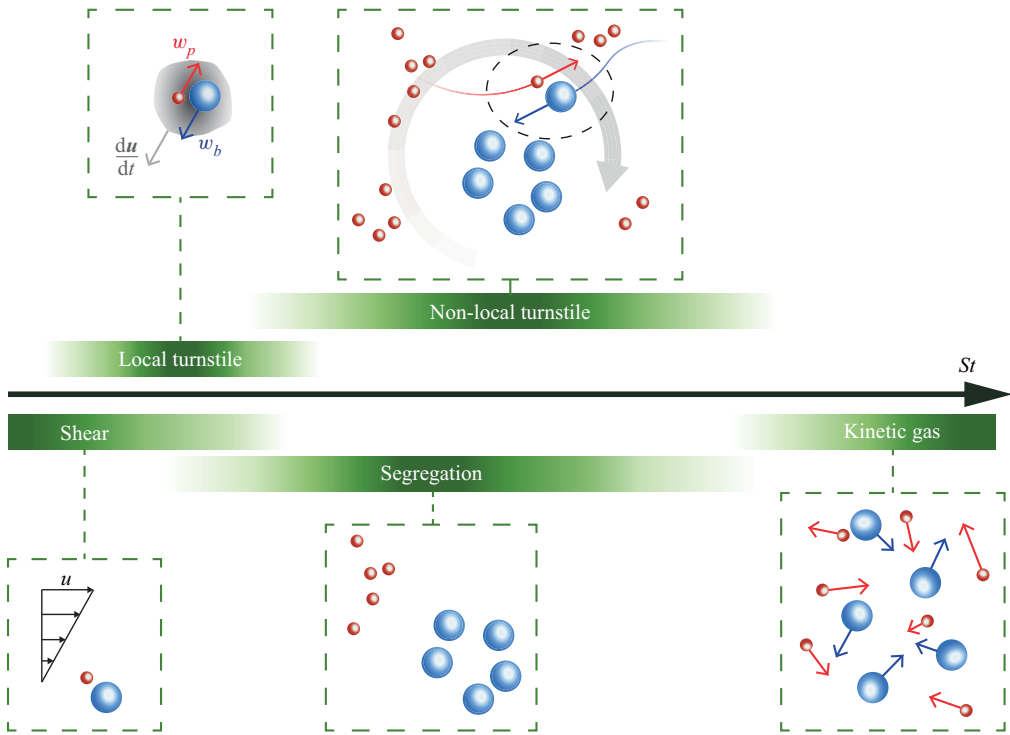
Figure 16. A sketch of the bubble–particle collision mechanisms with their approximate *St* dependence.

and the apparent improvement by adaptations of this framework is merely an artefact of using inconsistent velocity expressions. Our data for bubble–particle collisions are better approximated by the models of Saffman & Turner (1956) and Zaichik *et al.* (2010) when taking an additional correction for the inhomogeneous distribution into account. The predictions based on the theory of Zaichik *et al.* (2010) generally overestimate S_- and fail to reproduce the finding that S_-^{bp} is largest in the present parameter range when comparing across species. These observations are not affected when using a linear drag relation, i.e. $f_i = 1$ in (3.2), or in the limit $\rho_p/\rho_f \to \infty$ as shown in § 4.3. We therefore could not reproduce the good agreement with the Zaichik *et al.* (2010) theory for S_-^{bp} reported in Fayed & Ragab (2013). Potentially, this is due to different choices for St_b, which we set to equal to St_p, whereas this parameter is kept constant in Fayed & Ragab (2013).

In our simulations, we employ the non-dimensional control parameters *St* and Re_λ. In practice, the fluid and particle properties are controlled separately so using r_b, r_p and ε is more common. However, by definition, changing ε affects both *St* and Re_λ. To assess the overall effect, consider the region between $St = 0.1$ and $St = 0.5$, where the non-dimensional collision kernel $\Gamma_{bp}\tau_\eta/r_c^3$ decreases most sharply and drops by a factor of approximately 1.3. As the particle parameters are constant, $\tau_i = $ const., this is associated with a 5-fold decrease in τ_η. According to the shear scaling, which appears to be applicable to our data, this increase in turbulence intensity implies also a 5-fold increase in Γ_{bp}. Hence there remains a net benefit from increasing the turbulence intensity even in this range, although the effect is reduced somewhat due to segregation.

Our results show that considering finite particle density, nonlinear drag and the lift force have limited effect on the bubble–particle collision rate. However, other relevant factors

are yet to be explored. Most importantly, this concerns the buoyancy force and finite size effects in particular for the bubble motion and non-identical *St* for bubbles and particles, as well as modelling the collision behaviour of bubbles and particles. More complex simulations as well as experiments are certainly needed to make precise predictions of the bubble–particle collision rate in realistic settings. However, as far as modelling approaches and a physical understanding are concerned, we believe that the most promising approach to disentangle the effect of additional factors (such as buoyancy) is to treat them as modifications to a simpler base case like the one studied here.

Author ORCIDs.

Timothy T.K. Chan https://orcid.org/0000-0003-2363-0403;

Chong Shen Ng https://orcid.org/0000-0002-4643-4192;

Dominik Krug https://orcid.org/0000-0002-0627-5676.

Appendix A. Extension of the Kruis & Kusters (1997) model to particles with different densities

The original model by Kruis & Kusters (1997) is applicable to collisions of particles with arbitrary but equal density only. Here, we extend their framework to collisions of particles with different densities. In their model, Kruis & Kusters (1997) considered two limits: small and large *St*. We follow their approach to derive the corresponding expressions for particles with different densities. For convenience, we first rewrite (3.2) as

$$\frac{\mathrm{d}\boldsymbol{v}_i}{\mathrm{d}t} = \gamma_i \frac{\mathrm{D}\boldsymbol{u}}{\mathrm{D}t} + \frac{\boldsymbol{u} - \boldsymbol{v}_i}{\tau_i}, \tag{A1}$$

where $\gamma_i = 3\rho_f/(2\rho_i + \rho_f)$ and $i = 1, 2$ as in § 1.

A.1. *Small St limit*

For small *St*, Kruis & Kusters (1997) based their model on Yuu (1984), which considers a 'local' inertial effect due to the different response to fluid fluctuations of particles having different *St* (originally termed the 'accelerative mechanism' in Kruis & Kusters (1997)) and the shear mechanism. The main contribution by Kruis & Kusters (1997) is employing a more accurate expression of the fluid Eulerian energy spectrum that also captures the dissipation range behaviour

$$E_f(\omega) = \frac{4u'^2\xi}{2\pi(\xi - 1)} \left(\frac{T_{fL}}{1 + T_{fL}^2\omega^2} - \frac{T_{fL}}{\xi^2 + T_{fL}^2\omega^2} \right), \tag{A2}$$

where ω is the angular frequency,

$$\xi = 2\left(\frac{T_{fL}}{\tau_L}\right)^2, \tag{A3}$$

$T_{fL} = 0.4L_f/u'$ is the fluid Lagrangian integral time scale, L_f is the Eulerian longitudinal integral length scale, and $\tau_L^2 = 2u'^2/\langle(\mathrm{D}u/\mathrm{D}t)^2\rangle = 2u'^2/(1.16\varepsilon^{3/2}\nu^{-1/2})$ is the square of the Lagrangian time scale.

For the local inertial effect, the ensemble average of the square of the collision velocity is

$$\langle[(\Delta v)_{12}^{(loc)}]^2\rangle = v_1'^2 + v_2'^2 - 2\langle v_1 v_2\rangle, \tag{A4}$$

where $\langle\cdot\rangle$ denotes ensemble averaging, and

$$v_i^2 = u'^2 \frac{\xi}{\xi - 1}\left[\frac{1 + \gamma_i^2\tau_i/T_{fL}}{1 + \tau_i/T_{fL}} - \frac{1 + \gamma_i^2\xi\tau_i/T_{fL}}{\xi(1 + \xi\tau_i/T_{fL})}\right] \tag{A5}$$

as derived in Kruis & Kusters (1997). The integral giving the particle velocity correlation term follows Yuu (1984), whose model has been extended to particles with unequal densities in Ngo-Cong *et al.* (2018). The integral in Ngo-Cong *et al.* (2018) reads

$$\langle v_1 v_2\rangle = \int_0^{+\infty} \frac{(\tau_1^{-2} + \gamma_1\omega^2)(\tau_2^{-2} + \gamma_2\omega^2) + \tau_1^{-1}\tau_2^{-1}(\gamma_1 - 1)(\gamma_2 - 1)\omega^2}{(\tau_1^{-2} + \omega^2)(\tau_2^{-2} + \omega^2)} E_f(\omega)\, \mathrm{d}\omega. \tag{A6}$$

Note that although Kruis & Kusters (1997) found a misprint in the integral given by Yuu (1984), this error has not propagated to Ngo-Cong *et al.* (2018). Performing the integration yields

$$\frac{\langle v_1 v_2\rangle}{u'^2} = 1 + \frac{\xi}{(\xi - 1)(\tau_1^{-1} + \tau_2^{-1})}\left[\frac{(\gamma_1 - 1)(\tau_2^{-1} + \tau_1^{-1}\gamma_2)}{1 + \tau_1^{-1}T_{fL}} + \frac{(\tau_1^{-1} + \tau_2^{-1}\gamma_1)(\gamma_2 - 1)}{1 + \tau_2^{-1}T_{fL}}\right.$$
$$\left. - \frac{(\gamma_1 - 1)(\tau_2^{-1} + \tau_1^{-1}\gamma_2)}{\tau_1^{-1}T_{fL} + \xi} - \frac{(\tau_1^{-1} + \tau_2^{-1}\gamma_1)(\gamma_2 - 1)}{\tau_2^{-1}T_{fL} + \xi}\right], \tag{A7}$$

which is different from the corresponding expression in Ngo-Cong *et al.* (2018) solely because of the usage of another form of $E_f(\omega)$ as given by (A2) in (A6).

For the collision velocity due to the shear mechanism, Kruis & Kusters (1997) used the result in Yuu (1984):

$$\langle[(\Delta v)_{12}^{(shr)}]^2\rangle = \frac{\varepsilon}{5\nu}\left(\frac{v_1'^2}{u'^2}r_1^2 + \frac{v_2'^2}{u'^2}r_2^2 + 2\frac{\langle v_1 v_2\rangle}{u'^2}r_1 r_2\right). \tag{A8}$$

Using (1.5) and allowing $\gamma_1 \neq \gamma_2$ gives

$$\langle[(\Delta v)_{12}^{(shr)}]^2\rangle = \frac{3\varepsilon}{5}\left(\frac{v_1'^2}{u'^2}\frac{\tau_1}{\gamma_1} + \frac{v_2'^2}{u'^2}\frac{\tau_2}{\gamma_2} + 2\frac{\langle v_1 v_2\rangle}{u'^2}\sqrt{\frac{\tau_1\tau_2}{\gamma_1\gamma_2}}\right). \tag{A9}$$

The overall collision kernel is then given by

$$\Gamma_{12} = \sqrt{8\pi}\, r_c^2\sqrt{\langle[(\Delta v)_{12}^{(loc)}]^2\rangle + \langle[(\Delta v)_{12}^{(shr)}]^2\rangle}. \tag{A10}$$

Note that in contrast to the expression in Kruis & Kusters (1997), (A10) does not carry a factor $1/\sqrt{3}$ as u' is defined as the single-component r.m.s. fluid velocity.

959 A6-24

A.2. *Large St limit*

The Kruis & Kusters (1997) expression of Γ for large St is essentially based on Williams & Crane (1983) except that the added mass term is retained. As in § A.1, the densities of the different species γ_i are assumed to be distinct. In this limit, the shear mechanism is not considered, so

$$\langle (\Delta v)^2_{12} \rangle = v'^2_1 + v'^2_2 - 2 \langle v_1 v_2 \rangle \tag{A11}$$

and

$$\Gamma_{12} = \sqrt{8\pi}\, r_c^2 \sqrt{\langle (\Delta v)^2_{12} \rangle}. \tag{A12}$$

Furthermore, a simpler version of $E_f(\omega)$, namely

$$E_f(\omega) = \frac{4u'^2}{2\pi} \left(\frac{T_{fL}}{1 + T_{fL}^2 \omega^2} \right) \tag{A13}$$

is used, which corresponds to an exponentially decaying fluid velocity autocorrelation function 'moving with the mean flow' $R_E^*(t) = \exp(-|t|/T_{fL})$ that does not account for the dissipation range. Kruis & Kusters (1997) showed that

$$v'^2_i = u'^2 \frac{1 + \gamma_i^2 \tau_i / T_{fL}}{1 + \tau_i / T_{fL}}, \tag{A14}$$

which leaves only the particle velocity correlation to be determined.

To determine $\langle v_1 v_2 \rangle$, we integrate (A1) for $t \in (-\infty, 0]$ and exercise the freedom that $t = 0$ can be chosen at any instant, to obtain

$$v_{ij}(\boldsymbol{x_i}, t) = \gamma_i\, u_{ij}(\boldsymbol{x_i}, t) + \frac{1 - \gamma_i}{\tau_i} \int_0^{+\infty} u_{ij}(\boldsymbol{x_i}, t - \phi) \exp\left(-\frac{\phi}{\tau_i} \right) \mathrm{d}\phi, \tag{A15}$$

where $j = x, y, z$ are the individual components of the corresponding vector, and $\boldsymbol{x_i}$ is the position vector. Then using the approximation (Williams & Crane 1983)

$$\langle u(\boldsymbol{x_1}, t')\, u(\boldsymbol{x_2}, t'') \rangle \approx R_E^*(t' - t'') \int_0^{+\infty} E_f(\omega) \cos\left[\omega\, \widehat{\Delta v} \left(t - \frac{t' + t''}{2} \right) \right] \mathrm{d}\omega, \tag{A16}$$

where $\widehat{\Delta v}$ is a non-dimensional particle relative velocity, we have

$$\begin{aligned}
\langle v_1 v_2 \rangle = {} & \gamma_1 \gamma_2 u'^2 + \frac{(1 - \gamma_1)(1 - \gamma_2)}{\tau_1 \tau_2} \int_0^\infty \int_0^\infty \int_0^\infty \exp\left(-\frac{|\psi - \phi|}{T_{fL}} \right) \frac{2}{\pi} u'^2 \frac{T_{fL}}{1 + \omega^2 T_{fL}^2} \\
& \times \cos\left[\omega\, \widehat{\Delta v} \left(\frac{\psi + \phi}{2} \right) \right] \exp\left(-\frac{\psi}{\tau_1} - \frac{\phi}{\tau_2} \right) \mathrm{d}\omega\, \mathrm{d}\psi\, \mathrm{d}\phi \\
& + \frac{(1 - \gamma_1)\gamma_2}{\tau_1} \int_0^\infty \int_0^\infty \exp\left(-\frac{|\psi|}{T_{fL}} \right) \frac{2}{\pi} u'^2 \frac{T_{fL}}{1 + \omega^2 T_{fL}^2} \cos\left(\omega\, \widehat{\Delta v}\, \frac{\psi}{2} \right) \exp\left(-\frac{\psi}{\tau_1} \right) \mathrm{d}\omega\, \mathrm{d}\psi \\
& + \frac{\gamma_1(1 - \gamma_2)}{\tau_2} \int_0^\infty \int_0^\infty \exp\left(-\frac{|\phi|}{T_{fL}} \right) \frac{2}{\pi} u'^2 \frac{T_{fL}}{1 + \omega^2 T_{fL}^2} \cos\left(\omega\, \widehat{\Delta v}\, \frac{\phi}{2} \right) \exp\left(-\frac{\phi}{\tau_2} \right) \mathrm{d}\omega\, \mathrm{d}\phi.
\end{aligned} \tag{A17}$$

As $\tau_1, \tau_2 \gg 1$, $\exp(-\psi/\tau_1 - \phi/\tau_2) \approx 0$ except when $\psi = \phi$. Hence we retain this case only in the arguments of cosine and $\exp(-\psi/\tau_1 - \phi/\tau_2)$. Furthermore, we replace $\widehat{\Delta v}$ by
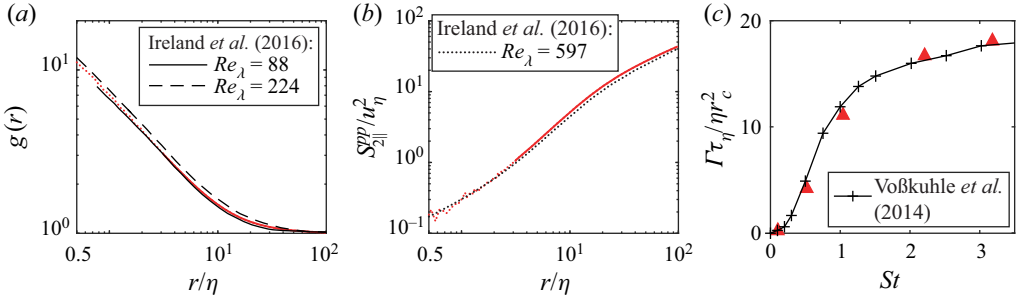
Figure 17. Particle–particle collision statistics of infinitely heavy particles: (*a*) the RDF $g_{pp}(r)$ at $St = 1$; (*b*) the variance of the radial component of the relative velocity $S_{2\parallel}^{pp}(r)$ at $St = 1$; and (*c*) the collision kernel Γ_{pp} when taking $\rho_p/\rho_f = 250$ and $r_c = 2r_p$.

$\widehat{\Delta v_X} = \sqrt{(v_1'^2 + v_2'^2)/u'^2}$ as the particle velocity correlation should be weak at large *St*. Thus

$$
\frac{\langle v_1 v_2 \rangle}{u'^2} = \gamma_1 \gamma_2 + \frac{(1 - \gamma_1)(1 - \gamma_2)}{\tau_1 \tau_2} \int_0^\infty \int_0^\infty \int_0^\infty \exp\left(-\frac{|\psi - \phi|}{T_{fL}}\right) \mathrm{d}\psi \; \frac{2T_{fL}}{\pi(1 + \omega^2 T_{fL}^2)}
$$

$$
\times \cos\left(\omega \, \widehat{\Delta v_X} \, \phi\right) \exp\left[-\phi\left(\frac{1}{\tau_1} + \frac{1}{\tau_2}\right)\right] \mathrm{d}\omega \, \mathrm{d}\phi
$$

$$
+ \frac{(1 - \gamma_1)\gamma_2}{\tau_1} \int_0^\infty \int_0^\infty \exp\left(-\frac{|\psi|}{T_{fL}}\right) \frac{2T_{fL}}{\pi(1 + \omega^2 T_{fL}^2)} \cos\left(\omega \, \widehat{\Delta v_X} \, \frac{\psi}{2}\right) \exp\left(-\frac{\psi}{\tau_1}\right) \mathrm{d}\omega \, \mathrm{d}\psi
$$

$$
+ \frac{\gamma_1(1 - \gamma_2)}{\tau_2} \int_0^\infty \int_0^\infty \exp\left(-\frac{|\phi|}{T_{fL}}\right) \frac{2T_{fL}}{\pi(1 + \omega^2 T_{fL}^2)} \cos\left(\omega \, \widehat{\Delta v_X} \, \frac{\phi}{2}\right) \exp\left(-\frac{\phi}{\tau_2}\right) \mathrm{d}\omega \, \mathrm{d}\phi.
$$

$$(A18)$$

Integrating first over ω and then the remaining variables finally results in

$$
\frac{\langle v_1 v_2 \rangle}{u'^2} = T_{fL} \frac{(1 - \gamma_1)(1 - \gamma_2)}{\tau_1 \tau_2} \left[\frac{2}{\tau_1^{-1} + \tau_2^{-1} + \widehat{\Delta v_X} \, T_{fL}^{-1}} - \left(\frac{1}{\tau_1} + \frac{1}{\tau_2} + \frac{\widehat{\Delta v_X} + 1}{T_{fL}}\right)^{-1} \right]
$$

$$
+ \frac{(1 - \gamma_1)\gamma_2}{\tau_1} \left(\frac{1}{T_{fL}} + \frac{1}{\tau_1} + \frac{\widehat{\Delta v_X}}{2T_{fL}}\right)^{-1} + \frac{\gamma_1(1 - \gamma_2)}{\tau_2} \left(\frac{1}{T_{fL}} + \frac{1}{\tau_2} + \frac{\widehat{\Delta v_X}}{2T_{fL}}\right)^{-1}
$$

$$
+ \gamma_1 \gamma_2.
$$

$$(A19)$$

Appendix B. Verification of point-particle code

To verify our code for the suspended phase, we compared the results of the infinitely heavy particle cases to the literature. As demonstrated by figure 17, the RDF $g(r)$, the variance of the radial component of the relative velocity $S_{2\parallel}^{pp}(r)$ as defined by (4.1), and the collision kernel Γ agree very well with data from Ireland *et al.* (2016) and Voßkuhle *et al.* (2014), especially considering the difference in Re_λ compared to the literature data in figures 17(*a*,*b*).
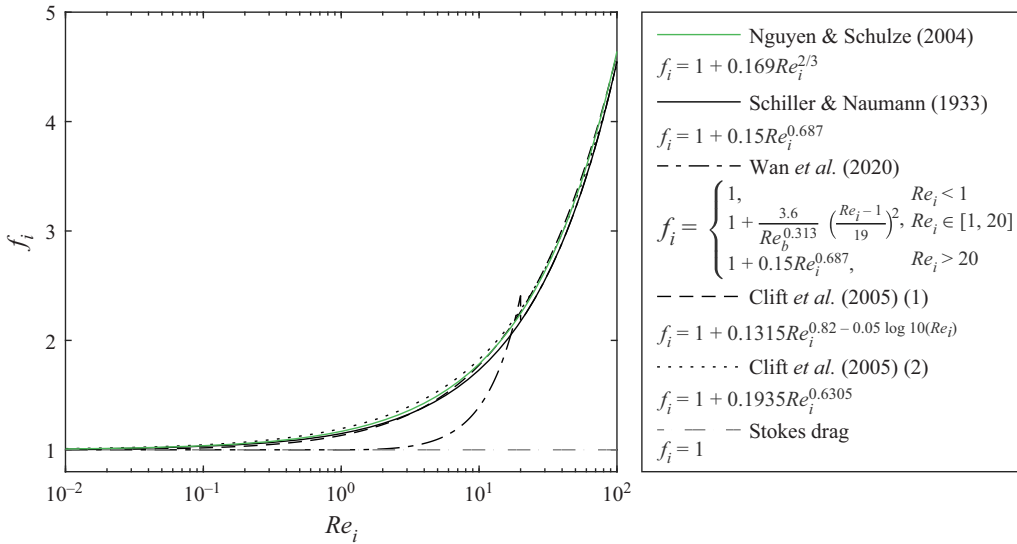
Figure 18. Various drag correction factors f_i from the literature compared to the one by Nguyen & Schulze (2004) used in this study (solid green line).

Appendix C. Comparison of different drag parametrisations

Various expressions of the drag correction factor f_i have been proposed in the literature. Figure 18 shows that they are mostly similar for $Re_i \lesssim 100$.

REFERENCES

ABRAHAMSON, J. 1975 Collision rates of small particles in a vigorously turbulent fluid. *Chem. Engng Sci.* **30** (11), 1371–1379.

ALISEDA, A., CARTELLIER, A., HAINAUX, F. & LASHERAS, J.C. 2002 Effect of preferential concentration on the settling velocity of heavy particles in homogeneous isotropic turbulence. *J. Fluid Mech.* **468**, 77–105.

BEC, J., BIFERALE, L., CENCINI, M., LANOTTE, A., MUSACCHIO, S. & TOSCHI, F. 2007 Heavy particle concentration in turbulence at dissipative and inertial scales. *Phys. Rev. Lett.* **98** (8), 084502.

BEC, J., CELANI, A., CENCINI, M. & MUSACCHIO, S. 2005 Clustering and collisions of heavy particles in random smooth flows. *Phys. Fluids* **17** (7), 073301.

BEWLEY, G.P., SAW, E.-W. & BODENSCHATZ, E. 2013 Observation of the sling effect. *New J. Phys.* **15**, 083051.

BLOOM, F. & HEINDEL, T.J. 2002 On the structure of collision and detachment frequencies in flotation models. *Chem. Engng Sci.* **57** (13), 2467–2473.

BRANDT, L. & COLETTI, F. 2022 Particle-laden turbulence: progress and perspectives. *Annu. Rev. Fluid Mech.* **54** (1), 159–189.

CALZAVARINI, E., CENCINI, M., LOHSE, D. & TOSCHI, F. 2008*a* Quantifying turbulence-induced segregation of inertial particles. *Phys. Rev. Lett.* **101** (8), 084504.

CALZAVARINI, E., KERSCHER, M., LOHSE, D. & TOSCHI, F. 2008*b* Dimensionality and morphology of particle and bubble clusters in turbulent flow. *J. Fluid Mech.* **607**, 13–24.

CHEN, L., GOTO, S. & VASSILICOS, J.C. 2006 Turbulent clustering of stagnation points and inertial particles. *J. Fluid Mech.* **553**, 143–154.

CHOUIPPE, A. & UHLMANN, M. 2015 Forcing homogeneous turbulence in direct numerical simulation of particulate flow with interface resolution and gravity. *Phys. Fluids* **27** (12), 123301.

CLIFT, R., GRACE, J. & WEBER, M.E. 2005 *Bubbles, Drops, and Particles*. Dover.

COLEMAN, S.W. & VASSILICOS, J.C. 2009 A unified sweep-stick mechanism to explain particle clustering in two- and three-dimensional homogeneous, isotropic turbulence. *Phys. Fluids* **21** (11), 113301.

DARABI, H., KOLEINI, S.M.J., DEGLON, D., REZAI, B. & ABDOLLAHY, M. 2019 Investigation of bubble–particle interactions in a mechanical flotation cell. Part 1: collision frequencies and efficiencies. *Miner. Engng* **134**, 54–64.

ESWARAN, V. & POPE, S.B. 1988 An examination of forcing in direct numerical simulations of turbulence. *Comput. Fluids* **16** (3), 257–278.

FALKOVICH, G., FOUXON, A. & STEPANOV, M.G. 2002 Acceleration of rain initiation by cloud turbulence. *Nature* **419** (6903), 151–154.

FALKOVICH, G. & PUMIR, A. 2007 Sling effect in collisions of water droplets in turbulent clouds. *J. Atmos. Sci.* **64** (12), 4497–4505.

FAYED, H.E. & RAGAB, S.A. 2013 Direct numerical simulation of particles–bubbles collisions kernel in homogeneous isotropic turbulence. *J. Comput. Multiphase Flows* **5** (3), 167–188.

FOUXON, I. 2012 Distribution of particles and bubbles in turbulence at a small Stokes number. *Phys. Rev. Lett.* **108** (13), 134502.

GOTO, S. & VASSILICOS, J.C. 2006 Self-similar clustering of inertial particles and zero-acceleration points in fully developed two-dimensional turbulence. *Phys. Fluids* **18** (11), 115103.

GOTO, S. & VASSILICOS, J.C. 2008 Sweep-stick mechanism of heavy particle clustering in fluid turbulence. *Phys. Rev. Lett.* **100** (5), 054503.

HASSANZADEH, A., FIROUZI, M., ALBIJANIC, B. & CELIK, M.S. 2018 A review on determination of particle–bubble encounter using analytical, experimental and numerical methods. *Miner. Engng* **122**, 296–311.

VAN HINSBERG, M.A.T., CLERCX, H.J.H. & TOSCHI, F. 2017 Enhanced settling of nonheavy inertial particles in homogeneous isotropic turbulence: the role of the pressure gradient and the Basset history force. *Phys. Rev.* E **95** (2), 023106.

HOMANN, H. & BEC, J. 2010 Finite-size effects in the dynamics of neutrally buoyant particles in turbulent flow. *J. Fluid Mech.* **651**, 81–91.

HUANG, Z., LEGENDRE, D. & GUIRAUD, P. 2012 Effect of interface contamination on particle–bubble collision. *Chem. Engng Sci.* **68** (1), 1–18.

IJZERMANS, R.H.A., MENEGUZ, E. & REEKS, M.W. 2010 Segregation of particles in incompressible random flows: singularities, intermittency and random uncorrelated motion. *J. Fluid Mech.* **653**, 99–136.

IRELAND, P.J., BRAGG, A.D. & COLLINS, L.R. 2016 The effect of Reynolds number on inertial particle dynamics in isotropic turbulence. Part 1. Simulations without gravitational effects. *J. Fluid Mech.* **796**, 617–658.

JIMÉNEZ, J., WRAY, A.A., SAFFMAN, P.G. & ROGALLO, R.S. 1993 The structure of intense vorticity in isotropic turbulence. *J. Fluid Mech.* **255**, 65–90.

KOLMOGOROV, A.N. 1941 The local structure of turbulence in incompressible viscous fluid for very large Reynolds number. *Dokl. Akad. Nauk USSR* **30**, 299–303.

KOLMOGOROV, A.N. 1963 On the approximation of distributions of sums of independent summands by infinitely divisible distributions. *Sankhyā* **25** (2), 159–174.

KOSTOGLOU, M., KARAPANTSIOS, T.D. & EVGENIDIS, S. 2020*a* On a generalized framework for turbulent collision frequency models in flotation: the road from past inconsistencies to a concise algebraic expression for fine particles. *Adv. Colloid Interface Sci.* **284**, 102270.

KOSTOGLOU, M., KARAPANTSIOS, T.D. & OIKONOMIDOU, O. 2020*b* A critical review on turbulent collision frequency/efficiency models in flotation: unravelling the path from general coagulation to flotation. *Adv. Colloid Interface Sci.* **279**, 102158.

KRUIS, F.E. & KUSTERS, K.A. 1997 The collision rate of particles in turbulent flow. *Chem. Engng Commun.* **158** (1), 201–230.

LI, J., ABRAHAM, A., GUALA, M. & HONG, J. 2021 Evidence of preferential sweeping during snow settling in atmospheric turbulence. *J. Fluid Mech.* **928**, A8.

LIEPE, F. & MÖCKEL, H.-O. 1976 Untersuchungen zum stoffvereinigen in flüssiger phase. *Chem. Technol.* **28** (4), 205–209.

MAXEY, M.R. 1987 The gravitational settling of aerosol particles in homogeneous turbulence and random flow fields. *J. Fluid Mech.* **174**, 441–465.

MAXEY, M.R. & RILEY, J.J. 1983 Equation of motion for a small rigid sphere in a nonuniform flow. *Phys. Fluids* **26** (4), 883–889.

MAZZITELLI, I.M., LOHSE, D. & TOSCHI, F. 2003 The effect of microbubbles on developed turbulence. *Phys. Fluids* **15** (1), L5.

MEHLIG, B., USKI, V. & WILKINSON, M. 2007 Colliding particles in highly turbulent flows. *Phys. Fluids* **19** (9), 098107.

MIETTINEN, T., RALSTON, J. & FORNASIERO, D. 2010 The limits of fine particle flotation. *Miner. Engng* **23** (5), 420–437.

MONCHAUX, R., BOURGOIN, M. & CARTELLIER, A. 2010 Preferential concentration of heavy particles: a Voronoï analysis. *Phys. Fluids* **22** (10), 103304.

NGO-CONG, D., NGUYEN, A.V. & TRAN-CONG, T. 2018 Isotropic turbulence surpasses gravity in affecting bubble–particle collision interaction in flotation. *Miner. Engng* **122**, 165–175.

NGUYEN, A.V., AN-VO, D.-A., TRAN-CONG, T. & EVANS, G.M. 2016 A review of stochastic description of the turbulence effect on bubble–particle interactions in flotation. *Intl J. Miner. Process.* **156**, 75–86.

NGUYEN, A.V., GEORGE, P. & JAMESON, G.J. 2006 Demonstration of a minimum in the recovery of nanoparticles by flotation: theory and experiment. *Chem. Engng Sci.* **61** (8), 2494–2509.

NGUYEN, A.V. & SCHULZE, H.J. 2004 *Colloidal Science of Flotation*, 1st edn. Surfactant Sciences, vol. 118. CRC.

OBLIGADO, M., TEITELBAUM, T., CARTELLIER, A., MININNI, P. & BOURGOIN, M. 2014 Preferential concentration of heavy particles in turbulence. *J. Turbul.* **15** (5), 293–310.

OSTILLA-MONICO, R., YANG, Y., VAN DER POEL, E.P., LOHSE, D. & VERZICCO, R. 2015 A multiple-resolution strategy for direct numerical simulation of scalar turbulence. *J. Comput. Phys.* **301**, 308–321.

PETERSEN, A.J., BAKER, L. & COLETTI, F. 2019 Experimental study of inertial particles clustering and settling in homogeneous turbulence. *J. Fluid Mech.* **864**, 925–970.

VAN DER POEL, E.P., OSTILLA-MÓNICO, R., DONNERS, J. & VERZICCO, R. 2015 A pencil distributed finite difference code for strongly turbulent wall-bounded flows. *Comput. Fluids* **116**, 10–16.

PUMIR, A. & WILKINSON, M. 2016 Collisional aggregation due to turbulence. *Annu. Rev. Condens. Matter Phys.* **7**, 141–170.

ROGICH, D.G. & MATOS, G.R. 2008 The global flows of metals and minerals. Open-File Report 2008-1355. U.S. Geological Survey.

SAFFMAN, P.G. & TURNER, J.S. 1956 On the collision of drops in turbulent clouds. *J. Fluid Mech.* **1** (1), 16–30.

SAW, E.W. 2008 Studies of spatial clustering of inertial particles in turbulence. PhD thesis, Michigan Technological University, Houghton, MI.

SCHILLER, L. & NAUMANN, A.Z. 1933 Über die grundlegenden berechnungen bei der schwerkraftauf-bereitung. *Z. Verein. Deutsch. Ing.* **77** (12), 318–320.

SCHUBERT, H. 1999 On the turbulence-controlled microprocesses in flotation machines. *Intl J. Miner. Process.* **56** (1), 257–276.

SPANDAN, V., PUTT, D., OSTILLA-MÓNICO, R. & LEE, A.A. 2020 Fluctuation-induced force in homogeneous isotropic turbulence. *Sci. Adv.* **6** (14), eaba0461.

SUNDARAM, S. & COLLINS, L.R. 1996 Numerical considerations in simulating a turbulent suspension of finite-volume particles. *J. Comput. Phys.* **124** (2), 337–350.

SUNDARAM, S. & COLLINS, L.R. 1997 Collision statistics in an isotropic particle-laden turbulent suspension. Part 1. Direct numerical simulations. *J. Fluid Mech.* **335**, 75–109.

TCHEN, C.-M. 1947 Mean value and correlation problems connected with the motion of small particles suspended in a turbulent fluid. PhD thesis, Technische Hogeschool Delft, Delft.

VERZICCO, R. & ORLANDI, P. 1996 A finite-difference scheme for three-dimensional incompressible flows in cylindrical coordinates. *J. Comput. Phys.* **123** (2), 402–414.

VÖLK, H.J., JONES, F.C., MORFILL, G.E. & RÖSER, S. 1980 Collisions between grains in a turbulent gas. *Astron. Astrophys.* **85** (3), 316–325.

VOßKUHLE, M., PUMIR, A., LÉVÊQUE, E. & WILKINSON, M. 2014 Prevalence of the sling effect for enhancing collision rates in turbulent suspensions. *J. Fluid Mech.* **749**, 841–852.

WAN, D., YI, X., WANG, L.-P., SUN, X., CHEN, S. & WANG, G. 2020 Study of collisions between particles and unloaded bubbles with point-particle model embedded in the direct numerical simulation of turbulent flows. *Miner. Engng* **146**, 106137.

WANG, L.-P., AYALA, O. & XUE, Y. 2005 Reconciling the cylindrical formulation with the spherical formulation in the kinematic descriptions of collision kernel. *Phys. Fluids* **17** (6), 067103.

WANG, X., WAN, M., YANG, Y., WANG, L.-P. & CHEN, S. 2020 Reynolds number dependence of heavy particles clustering in homogeneous isotropic turbulence. *Phys. Rev. Fluids* **5** (12), 124603.

WANG, L.-P., WEXLER, A.S. & ZHOU, Y. 1998 On the collision rate of small particles in isotropic turbulence. I. Zero-inertia case. *Phys. Fluids* **10** (1), 266–276.

WILKINSON, M., MEHLIG, B. & BEZUGLYY, V. 2006 Caustic activation of rain showers. *Phys. Rev. Lett.* **97** (4), 048501.

WILLIAMS, J.J.E. & CRANE, R.I. 1983 Particle collision rate in turbulent flow. *Intl J. Multiphase Flow* **9** (4), 421–435.

WORLD BANK GROUP 2017 *The Growing Role of Minerals and Metals for a Low Carbon Future*. World Bank.

YUU, S. 1984 Collision rate of small particles in a homogeneous and isotropic turbulence. *AIChE J.* **30** (5), 802–807.

ZAICHIK, L.I. & ALIPCHENKOV, V.M. 2009 Statistical models for predicting pair dispersion and particle clustering in isotropic turbulence and their applications. *New J. Phys.* **11** (10), 103018.

ZAICHIK, L.I., SIMONIN, O. & ALIPCHENKOV, V.M. 2010 Turbulent collision rates of arbitrary-density particles. *Intl J. Heat Mass Transfer* **53** (9), 1613–1620.

ZHOU, Y., WEXLER, A.S. & WANG, L.-P. 2001 Modelling turbulent collision of bidisperse inertial particles. *J. Fluid Mech.* **433**, 77–104.